Inorg. Chem. **2004**, *43*, 1998–2012

DFT-Based Pseudo-Jahn–Teller Coupling Studies on the Steric and Energetic Lone Pair Effect of Four- and Five-Coordinate Halide Molecules and Complexes with Central Ions from the Fifth, Sixth, and Seventh Main Groups

M. Atanasov[†,‡] **and D. Reinen***[,‡]

Institute of General and Inorganic Chemistry, Bulgarian Academy of Sciences, 1113 Sofia, Bulgaria, and Fachbereich Chemie und Zentrum für Naturwissenschaften der Philipps-Universität, Hans-Meerweinstrasse 1, D-35043 Marburg, Germany

Received June 30, 2003

The energetical and stereochemical effect of the s^2 lone pair in the title molecules and complexes is investigated using a pseudo-Jahn–Teller coupling model with parameters adjusted to energies and wave functions from DFT calculations. Vibronic coupling parameters were calculated and compared with those of the coordination number (CN) 3. Inspecting the correlation between the chemical hardness and the vibronic coupling energy (*hardness rule*), it is found that the tendency to distort decreases with increasing CN. While all considered molecules AX_3 (A^{III} = P to Bi; X^- = F to I) undergo lone pair deformations ($D_{3h} \rightarrow C_{3v}$), only part of the AX_4^- and BX_4 species (B^{IV} = S to Po) do so ($T_d \rightarrow C_{2v}$)—and even less the ones with CN = 5 ($D_{3h} \rightarrow C_{2v}$ ($\cong C_{4v}$)), AX_5^{2-}, BX_5^-, and CF_5 (C^V; Cl to I). The distorted polyhedra of minimum energy possess usually the butterfly C_{2v} shape (CN = 4, $\tau_2(\zeta)$ displacement path) and a $C_{2v} = C_{4v}$ geometry (CN = 5, ϵ' (ϵ) distortion path). A further symmetry lowering to C_s occurs, if the central ion becomes too small with respect to the ligands (*ionic size influence*, $PCl(Br)_4^-$, PCl_5^{2-}), with the tendency to reduce the CN toward 3 + 1 and 4 + 1, respectively. For CN = 4 the various stationary points of, for example, compressed and elongated C_{3v}, C_{4v}, etc. in the multidimensional ground-state potential surface have been characterized. Though of higher energy than the absolute C_{2v} minimum, they are shown to govern the dynamics and reactivity of the CN = 4 species to a large extent. To simulate the chemical environment (positively charged counterions, polar solvents), the DFT calculations were performed using the polarizable continuum model COSMO (conductor-like screening model). Though the electronic energy gain upon distortion is not significantly affected by the solvent, the total stabilization energy is distinctly enhanced, frequently leading to lone pair deformations of otherwise electronically stable species. All results obtained by the combined vibronic/DFT approach are well in accord with available experimental data.

I. Introduction

The lone pair effect is a well-documented phenomenon in the stereochemistry of inorganic compounds, and it has been challenging to both experimentalists[1,2] and theoreticians[3] to understand and to instrumentalize the basic principles. Though the valence shell electron pair repulsion (VSEPR) model[4] can be used to interpret observed distortions, its predictive power is restricted: (i) Various lone pair systems—particularly with higher coordination numbers (CNs)—do not show any deviation from the high-symmetry parent structure (inert-pair effect). (ii) Deformations of complexes or mol-

* Author to whom correspondence should be addressed. Fax: +49 6421 2828917. E-mail: reinen@chemie.uni-marburg.de.
† Bulgarian Academy of Sciences.
‡ Philipps-Universität.

(1) Greenwood, N. N.; Earnshow, A. *Chemistry of the Elements*, 2nd ed.; Butterworth & Heinemann: Oxford, 1998.
(2) Wiberg, N. *Lehrbuch der Anorganischen Chemie*; Walter de Gruyter: Berlin, New York, 1995.
(3) Öpik, U.; Pryce, M. H. L. *Proc. R. Soc. London, Ser. A* **1957**, *238*, 425. Bader, R. F. W. *Can. J. Chem.* **1962**, *40*, 1164. Pearson, R. G. *J. Am. Chem. Soc.* **1969**, *91*, 4947. Bersuker, I. B. *Chem. Rev.* **2001**, *101*, 1067.
(4) Gillespie, R. J.; Nyholm, R. S. *Q. Rev. (London)* **1957**, *11*, 339. Gillespie, R. J.; Robinson, E. A. *Angew. Chem.* **1996**, *108*, 539; *Angew. Chem., Int. Ed. Engl.* **1996**, *35*, 495. Gillespie, R. J. *Coord. Chem. Rev.* **2000**, *197*, 51.

10.1021/ic030214s CCC: $27.50
Published on Web 02/05/2004

ecules possessing high CNs (≥ 6) cannot be unambiguously predicted using the simple VSEPR concept. (iii) No information about the distortion pathway is provided. (iv) The energetic origin of the lone pair effect remains obscure.

We present here results for halide molecules and complexes BX_4, AX_4^-, CX_5, BX_5^-, and AX_5^{2-}, where A, B, and C are cations from the fifth, sixth, and seventh main groups with the oxidation states III, IV, and V, respectively—derived from a DFT-parametrized vibronic coupling model of the pseudo-Jahn−Teller (PJT) type. Following this concept, some predictions about the stereochemical lone pair activity are possible: (i) In the case of AX_3 molecules, which we investigated previously,[5] the vibronic coupling energy dominates the lone pair effect and can be nicely correlated with the chemical hardness—which is an observable quantity; the harder the lone pair molecule, the more susceptible to distortion it becomes (*hardness rule*). (ii) First results for species with a larger number of ligands indicate that they become softer and resist lone pair distortions more the higher the CN.[6] (iii) The vibronic coupling effect has been found to be a nearly pure orbital overlap phenomenon; there is no energy stabilization via decreased electron pair repulsion in the distorted geometry, as claimed by the VESPR model. It is the interplay between the vibronic energy gain due to changes in the covalent bonding and the restoring energy (comprising the Pauli and Coulomb repulsion energies) which determines whether a distortion will take place or not.

In preceding studies we have used a vibronic model with linear and quadratic terms in the nuclear coordinates and have fitted its vibronic parameters to DFT data.[5,6] This method could be well applied to AX_3 molecules, but becomes very complex, due to the high degree of parametrization, for larger CNs. In the present study we apply an alternative method for extracting vibronic coupling energies[7] which is based on Slater's transition-state method.[8] It allows vibronic energies to be calculated from DFT results, without recourse to particular vibronic parametrizations based on a Herzberg−Teller energy expansion in terms of nuclear displacements.

The intention of this study is to supply the experimental chemist with at least approximate rules which allow to predict whether a lone pair molecule or complex will distort and if it does which geometry it adopts. In particular a correlation with fundamental quantities (chemical hardness,[9] the ionic-radius ratio,[10] etc.) is intended. In the case of charged species we will analyze how the electrostatic surrounding modifies the vibronic landscape and to what extent environmental effects contribute in stabilizing a distorted structure.

II. Theory

II.1. Vibronic Coupling Model. The tetrahedral geometry of say a molecule BX_4 might be unstable if the highest occupied molecular orbital (HOMO) of $a_1(s^2)$ type carrying the lone pair—which is usually antibonding and frequently strongly delocalized toward the ligands—interacts with the lowest unoccupied MO (LUMO) of t_2 symmetry originating from the p-orbitals of B, which is also (and even stronger) antibonding (see Figure 5). In a many-electron description the ground state ($...a_1^2$) and the singly excited state ($...a_1^1t_2^1$) configurations give rise to A_1 and T_2 states, respectively, which mix upon distortion of the tetrahedron. The way this occurs is dictated by the two stretching and bending τ_2 modes in T_d ($A_1 \otimes \tau_2 \otimes T_2$ coupling; see Figure 1 and matrix 1).[11] E_g

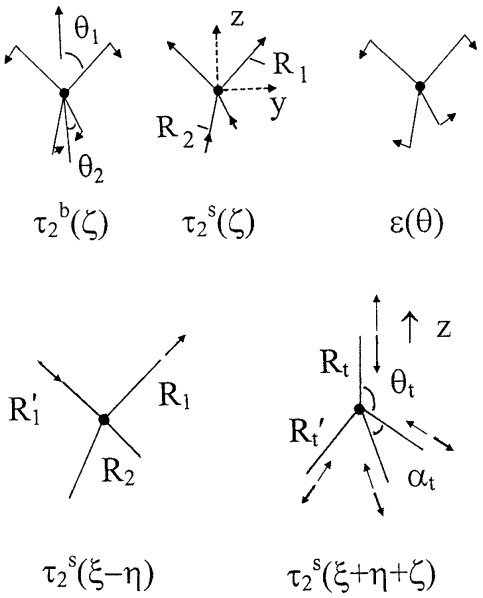

Figure 1. The higher-symmetry ζ components of the vibronically active vibrations in T_d (CN = 4): $\tau_2(\zeta)$ bending (b) and stretching (s) ($\rightarrow C_{2v}$) and $\epsilon(\theta)$ bending ($\rightarrow D_{2d}$) (top). Linear combinations of the τ_2^s stretching components $\xi + \eta + \zeta$ and $\xi - \eta$ leading to C_{3v} and *i*-C_{3v} (thick and thin lines) and C_s^a point groups, respectively (see the text) are also shown (bottom).

$$\begin{array}{c} \begin{matrix} A_1 & T_2^x & T_2^y & T_2^z \end{matrix} \\ \begin{bmatrix} E_g & N_x & N_y & N_z \\ N_x & E_e^x & P_{xy} & P_{xz} \\ N_y & P_{xy} & E_e^y & P_{yz} \\ N_z & P_{xz} & P_{yz} & E_e^z \end{bmatrix} \end{array} \qquad (1)$$

and E_e^x, E_e^y, and E_e^z are the energies of the A_1 and T_2 states, respectively, while N_x, N_y, and N_z parametrize the mixing of these states due to the τ_2-type distortion; *x*, *y*, and *z* correlate with the tetrahedral S_4^x, S_4^y, and S_4^z axes, and T_2^x, T_2^y, and T_2^z denote the corresponding excited-state wave functions. E_e^x, E_e^y, and E_e^z may differ due to a (diagonal) excited-state Jahn−Teller interaction via the ϵ vibration ($T_2 \otimes \epsilon \otimes T_2$ coupling, Figure 1). P_{xy}, P_{xz}, and P_{yz} are off-diagonal energies introduced to account for a $T_2 \otimes \tau_2 \otimes T_2$ excited-state Jahn−Teller interaction, which is also possible by symmetry. As was shown previously,[11] the excited-state JT interaction via the ϵ mode is essential in determining the topology of the ground-state potential surface, because excited-state properties are admixed to the ground state via the nondiagonal PJT

(5) Atanasov, M.; Reinen, D. *J. Phys. Chem. A* **2001**, *105*, 5450.
(6) Atanasov, M.; Reinen, D. *J. Am. Chem. Soc.* **2002**, *124*, 6693.
(7) Atanasov, M.; Reinen, D. *Adv. Quantum Chem.* **2003**, *44*, 355.
(8) Slater, J. C. *Adv. Quantum Chem.* **1972**, *6*, 1.
(9) Pearson, R. G. *Chemical Hardness*; Wiley-VCH: Weinheim, New York, **1997**.
(10) Wells, A. F. *Structural Inorganic Chemistry*, 5th ed.; Clarendon Press: Oxford, 1984; Chapter III.
(11) Maaskant, W. J. A.; Bersuker, I. B. *J. Phys.: Condens Matter* **1991**, *3*, 37.

Table 1. Vibronically Active Modes of Molecules and Complexes with s^2 Ground States in T_d (CN = 4) and D_{3h} (CN = 5) Symmetries[a]

symmetry	nuclear vibration	electronic wave function	symmetry	nuclear vibration	electronic wave function
CN = 4, T_d	τ_2	T_2	CN = 5, D_{3h}	ϵ', α_2''	E′, A_2''
C_{2v}	$\pm\varsigma$	T_2^z	C_{2v}	$\pm\epsilon$	E'_ϵ
C_{3v}	$\pm(1/\sqrt{3})(\xi+\eta+\varsigma)$	$(1/\sqrt{3})(T_2^x+T_2^y+T_2^z)$	C_s	$\pm\zeta$	E'_ζ
C_s	$\pm(1/\sqrt{2})(\xi-\eta)$	$(1/\sqrt{2})(T_2^x-T_2^y)$	C_{3v}	$\pm\alpha_2''$	A_2''

[a] The excited-state T_2 and E′ (A_2'') wave functions and those components which become totally symmetric in the distorted C_{2v}, C_{3v}, and C_s[a] (see the text) and C_{2v},C_s, and C_{3v} geometries, respectively, are also listed.

elements *N*. In Table 1 and Figure 1 we specify nuclear displacements and corresponding electronic wave functions pertaining to C_{2v}, C_{3v}, and C_s point groups—the highest possible distortion symmetries within the τ_2 component manifold. There are six (C_{2v}), eight (C_{3v}), and six (C_s) such combinations corresponding to the three S_4 and the four C_3 axes and the six symmetry planes (σ_s) of the parent tetrahedron. Excited states which are totally symmetric in one of the distorted geometries can thus mix into the $A_1(s^2)$ ground state, with the wave functions given in Table 1. Applying the formalism by Öpic and Price,[3] it is easy to show that, for C_{2v} and C_{3v} distortions, matrix 1 can be reduced to a 2 × 2 form (2), while C_s gives rise to a 3 × 3

$$\mathbf{H}_{C_{2v},C_{3v}} = \begin{bmatrix} E_g & N \\ N & E_e \end{bmatrix} \qquad (2)$$

matrix [A′ (A_1) and two A′ split components of T_2]. The energies E_e and *N* can be expressed by those of the original representation (matrix 1).[11] The topology of the ground-state potential surface and its energetic landscape, in particular stationary points of C_{2v}, C_{3v}, C_{4v}, and C_s geometry, have been explored for selected examples of s^2-type molecules by ab initio and DFT calculations of Moc and Morokuma[12] and more recently by Mauksch and von Schleyer.[13]

Turning to the vibronic coupling of species with CN = 5, we refer to matrix 1 again. Here the A_1' ground state of the parent D_{3h} geometry (with energy E_g) may interact with the lowest excited E′ state (with energy $E_e^x = E_e^y$)—see the Kohn−Sham MO scheme in Figure 11—via two bending (in-plane ϵ'_{ip} and out-of-plane ϵ'_{op}) vibrations and one stretching (ϵ'_s) vibration, and/or with the first A_2'' excited state (of energy E_e^z) via the bending α_2'' vibration (Figure 2)—$A_1'\otimes\epsilon'\otimes E'$ and $A_1'\otimes\alpha_2''\otimes A_2''$ coupling, respectively. While in the case of a trigonal planar (D_{3h}) environment (AX_3 molecules) the $a_2''(p_z)$ MO is the LUMO[5]—due to its only weakly π-antibonding character—this is different for the trigonal bipyramid, where the central ion p_z orbital is involved in strong axial σ bonds. Correspondingly, $e'(p_x,p_y)$ is the LUMO (Figure 11), because $A_2''(...s^1p_z^1)$ exceeds in energy the first excited $E'(...s^1p_{x,y}^1)$ state—for AX_5^{2-} complexes, for example, by between 1 eV (fluorides) and ∼0.3 eV (iodides). Furthermore, one has to consider the possible first-order Jahn−Teller interaction in the E′ excited state via the ϵ' modes ($E'\otimes\epsilon'\otimes E'$), which may modify the diagonal energies ($\rightarrow E_e^x \neq E_e^y$) considerably.[14] In Table 1 we specify

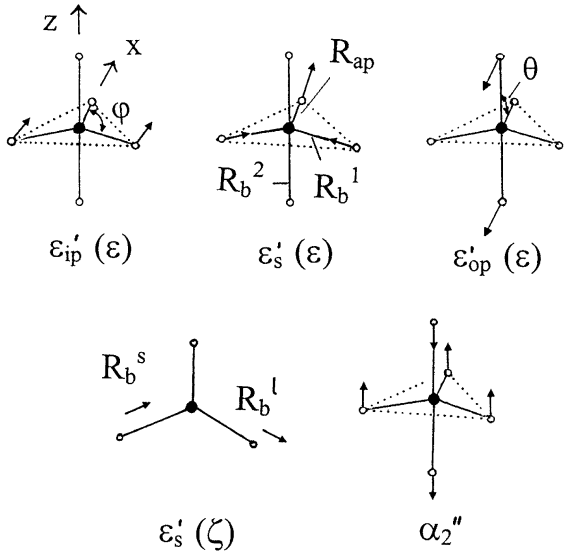

Figure 2. The higher-symmetry components of the vibronically active vibrations in D_{3h} with the bond lengths R_{eq} (3×) and R_{ax} (2×) (CN = 5): $\epsilon'(\epsilon)$ stretching (s), in-plane (ip) and out-of-plane (op) bending; indicated displacements for $\epsilon_s'(\epsilon)$ refer to *i*-C_{2v} and ligand movements inverse to the depicted directions to $C_{2v}(C_{4v})$ distortions (see the text) (top). Lower-symmetry $\epsilon_s'(\zeta)$-type stretching displacements (→C_s) and the α_2'' mode (→C_{3v}) are also shown (bottom).

nuclear displacements and corresponding electronic wave functions pertaining to C_{2v} (≅C_{4v})—the highest possible distortion symmetry induced by the action of ϵ'-type displacements—and to C_s, using the lower-symmetry components of the ϵ' modes (Figure 2). Inspecting the higher-symmetry distortion along one of the three C_2 axes, excited-state wave functions of p_x type become totally symmetric and can thus mix into the $A_1'(...s^2)$ ground state; matrix 1 simplifies to a 2 × 2 block diagonal form in that case (matrix 2). Allowing for a distortion of C_s symmetry (by the ζ components of the ϵ' modes), excited states of p_y type become additionally totally symmetric, leading to a 3 × 3 (s, p_x, p_y) matrix. Deformations of α_2'' type lead to a 2 × 2 (s, p_z) matrix, parametrizing the interaction between the $A_1'(...s^2)$ ground state and the $A_2''(...s^1p_z^1)$ excited state (Figure 2), and the symmetry decreases from D_{3h} to C_{3v}.

If strain influences from the higher-sphere environment are absent, distortions along an S_4 and C_2 axis in T_d (CN = 4) and D_{3h} (CN = 5), respectively, possess usually the lowest energies; hence, we have to refer to matrix 2 for further treatment. Here, E_g and E_e are the ground and excited many-electron states in the high-symmetry parent geometries T_d and D_{3h}, which are involved in the vibronic mixing induced by *N* ($E_e - E_g = \delta$, initial splitting). The general solution of matrix 2 is

(12) Moc, J.; Morokuma, K. *Inorg. Chem.* **1994**, *33*, 551.
(13) Mauksch, M.; Schleyer, P.v. R. *Inorg. Chem.* **2001**, *40*, 1756.
(14) Reinen, D.; Atanasov, M. *Chem. Phys.* **1989**, *136*, 27; **1991**, *155*, 157.

$$E_{-}{}^{m} = E_{rf}{}^{m} - E_{vib}{}^{m} \quad (3)$$

$$E_{vib}{}^{m} \equiv (1/2)(E_{FC}{}^{m} - \delta E_{g,e}{}^{m}) \quad (4a)$$

$$E_{FC}{}^{m} = E_{+}{}^{m} - E_{-}{}^{m} = 2[(\delta E_{g,e}{}^{m}/2)^2 + (N^m)^2]^{1/2} \quad (4b)$$

The total energy stabilization $E_{-}{}^{m}$ (DFT: $\equiv\delta E_t$) results from the difference of the vibronic ($E_{vib}{}^{m}$) and the restoring ($E_{rf}{}^{m}$) energies. Adopting the nomenclature of the DFT energy partition, the latter comprises (nearly) completely the electrostatic (δE_{el}) and the Pauli repulsion (δE_P) energies as well as that part of the orbital energy δE_{orb} which originates from the nuclear displacements accompanying the transition from the regular parent polyhedron to the distorted structure, *in case there would be no vibronic interaction* ($N = 0$).[5,6] It is usually (see below) >0, because otherwise a distortion would occur already without vibronic coupling. The energies $E_g{}^{m}$ and $E_e{}^{m}$ ($\delta E_{g,e}{}^{m} = E_e{}^{m} - E_g{}^{m}$) characterize the ground and excited states of the *distorted* polyhedron *before* the interaction via the nondiagonal element N occurs. The Franck−Condon energy $E_{FC}{}^{m}$ finally considers the increase of energy with respect to $\delta E_{g,e}{}^{m}$ by the vibronic coupling and determines via $E_{vib}{}^{m}$ (eqs 4a and 4b), whether a ground-state stabilization ($E_{-}{}^{m} < 0$) occurs or not (m denotes the energies of the DFT-optimized distorted structures). $E_{FC}{}^{m}$ has been shown to be directly connected with the chemical hardness of the distorted polyhedron (eq 5a), though the latter contains an additional significant interelectronic repulsion term C. In the case of strong vibronic coupling, where N^m dominates $E_{FC}{}^{m}$ (eq 4b), eq 5a simplifies to 5b.

$$\eta = (1/2)E_{FC}{}^{m} + C \quad (5a)$$

$$\eta \approx N^m + C \quad (5b)$$

AX_3 molecules—which are stable only in the distorted (pseudotetrahedral AX_3E) C_{3v} geometry—are more susceptible to lone pair distortions the harder they are. This hardness rule[5,6] implies a sequence from the soft iodide ligand to the hard fluorides via chloride and bromide and, in a much less pronounced way, from Bi^{III} to P^{III}. It can be shown (see the Appendix) that the repulsion term C follows—with very few exceptions—the same order, with increasing values from I^- to F^- and from Bi^{III} to P^{III}. After all, *the hardness rule relates the observable η to a not directly accessible quantity N^m, which represents the strength of the lone pair effect*.

In the case of charged molecules the total stabilization energies $\delta E_t = E_{-}{}^{m}$ are significantly influenced by additional electrostatic forces due to interactions with a solvent surrounding (in solution) or with counterions (in a crystalline lattice). In the DFT calculations such environmental disturbances are simulated by a polarizable continuum, with the dielectric constant of water, for example. Usually the solvent stabilizes the distorted entitites more than the high-symmetry parent complexes ($\delta E_{solv} < 0$), resulting in an additional energy gain ($\delta E_t < \delta E_t'$):

$$\delta E_t = \delta E_t' \ (\equiv E_{-}{}^{m}) + \delta E_{solv} \quad (6)$$

$\delta E_t'$ represents the pure *electronic* energy change during the transition from the high-symmetry to the distorted geometry. The solvent usually does not change the electronic structure of the complex very significantly.[15] If the stabilization energy of a molecule, say SCl_4, for the $T_d \rightarrow C_{2v}$ transition ($\delta E_t = -0.09$ eV) is compared with the corresponding electronic energy change for the solvated molecule $(SCl_4)_s$ ($\delta E_t' = 0.04$ eV), the difference is indeed rather small (see Table 3; here the solvent stabilizes $(SCl_4)_s$ in C_{2v}, $\delta E_{solv} = -0.37$ eV). One should further mention that the Franck−Condon energy $E_{FC}{}^{m}$ contains a solvent contribution, if the DFT calculation is performed in a solvent continuum, because the ground-state and the excited-state potential energy curves are differently influenced by the environmental disturbance. It cannot be separated from $E_{FC}{}^{m}$, but can be shown to be small and positive.[16] Thus, $E_{FC}{}^{m}$ and N^m for the solvated species represent "effective" values and are slightly larger than the true electronic quantities; however, this solvent effect does not essentially affect any conclusion from the vibronic model.

II.2. Calculation of the Vibronic Parameters. In treatments of the PJT effect a useful approximation has been to express the parameters N^m, $E_g{}^{m}$, and $E_e{}^{m}$ by linear and quadratic vibronic coupling terms[17,18] and fit these quantities to a database resulting from DFT calculations.[5,6] A more rigorous procedure has been developed recently,[7] following the Slater approximation.[8] It avoids the approximations inherent in the usual Herzberg−Teller exspansions of N^m, $E_g{}^{m}$, and $E_e{}^{m}$, and is applicable if only two interacting nondegenerate electronic states dominate the vibronic coupling. While the calculated N^m energies—on which all essential conclusions are based—are equal within narrow limits in the two approaches, $E_{rf}{}^{m}$ and $E_{vib}{}^{m}$ may differ considerably. The vibronic and restoring energies in Tables 6 and 10 are derived by applying Slater's transition-state theory.[8] They have to be considered to be more reliable than those (partly) published earlier (ref 5, Figures 6 and 9; ref 6, Figure 5).

Vibronic coupling becomes more complex if more than two electronic states couple with each other, as for a C_s distortion, for example. However, with the approximation that the lower-symmetry deformation can be treated as a perturbation superimposed on the dominating C_{2v} geometry, it is possible to deduce energy contributions $\delta E_{rf}{}^{m}$ and $\delta E_{vib}{}^{m}$, which characterize these additional polyhedron deformations.

II.3. Computational Details. The calculations in this paper have been performed using the Amsterdam Density Functional (ADF) program package (release 2002.03),[19] with the choice of the functionals described in refs 5 and 6. We used a triple-ζ (TZP) basis in all geometry optimizations and subsequent frequency calculations, with the exception of

(15) Atanasov, M.; Reinen, D. In *Comprehensive Coordination Chemistry II, Vol.1 Fundamentals*; Lever, A. B. P., Ed.; Elsevier: New York, 2003; Vol. 1, Chapter 1.36.
(16) Hush, N. S.; Reimers, J. R. *Chem. Rev.* **2000**, *100*, 775 and references therein.
(17) Bersuker, I. B. *The Jahn−Teller Effect and Vibronic Interactions in Modern Chemistry*; Plenum Press: New York, 1984.
(18) Bersuker, I. B. *Electronic Structure and Properties of Transition Metal Complexes*; John Wiley and Sons: New York, 1996; Chapter 9 and references therein.

$PF_n^{(n-3)-}$ ($n = 3-5$); here, we employed a double-ζ basis for P and F, however, because TZP calculations lead to two closely spaced virtual orbitals a_1, precluding a rigorous assignment of the LUMO. For the charged clusters AX_4^-, AX_5^{2-}, and BX_5^- and some BX_4 molecules we accounted for a solvent using the conductor-like screening model (COSMO)[20] as implemented in the ADF.[21] We chose the dielectric constant of H_2O ($\epsilon = 78.4$) with the solvent radius $R_{solv} = 1.4$ Å; for P, As, Sb, Bi, S, Se, and Te and F, Cl, Br, and I we used the solvent radii 2.40, 2.46, 2.67,2.88, 1.70, 2.53, and 2.74 and 1.40, 1.75, 1.85, and 1.98 Å, respectively. Geometry optimizations have been performed for various symmetries; all stationary points were checked with respect to the number of imaginary vibrational frequencies and hence to the existence of minima and saddle points of different order. In all calculations symmetry was utilized as much as possible, employing the option "ALLPOINTS" along with "INTEGRATION 5.0 5.0"—with reliable results, though comparatively long computational times. Otherwise convergence problems in the course of the geometry optimizations have been encountered in most cases. Optimized geometries, total energies, and vibrational frequencies can be supplied on request. Application of available density functionals to intermediate states in the course of dissociation processes (bond breaking) is sometimes critical and may affect the quality of the calculated data.[22] Despite this, we think the energies and geometric results are significant in the cases considered.

III. Results and Discussion

All complexes and molecules considered in this paper are calculated by DFT to be at stable energy minima in their ground-state geometries. The clear criterion is that every vibrational frequency of the respective point group possesses real values, which does not necessarily mean that the species are also thermodynamically stable. In turn imaginary frequencies for other stationary points indicate vibronic instability along the displacement vectors of the respective normal modes.

III.1. Coordination Number 4. In accord with the experimental evidence, the C_{2v}-type butterfly structure (Figure 1) is usually found to be the most stable from all possible distortion geometries (but see $(PCl_4^-)_s$ and $(PBr_4^-)_s$, discussed below). In contrast to the AX_3 molecules[5] some complexes and molecules are expected to persist as tetrahedra (Figure 3), however. In Table 2 we compare the rare structural data available from the literature with data from DFT. The agreement is satisfactory, though the calculated bond lengths are consistently about 3% too large. It is striking that the average bond length shrinks significantly when the tetrahedra are distorted—namely, by ~0.10(3) Å in the cases listed in Table 2. This has to be traced back to the p_z admixture to the $A_1(...s^2)$ ground state by the vibronic interaction;[5,6] the ligand repulsion by the s^2 lone pair is diminished in this way, because the p_z orbital orients such that it avoids the coordinated ligands. We notice the participation of three tetrahedral vibrations in the $T_d \rightarrow C_{2v}$ distortion process: these are the symmetry-breaking τ_2 modes (ζ components) and, in addition, the θ component of the Jahn–Teller mode, which causes a compression of the tetrahedron along the S_4 axis and would induce a D_{2d} distortion if present alone (Figure 1). The mentioned decrease of the mean A(B)–X distance from T_d to C_{2v} and the associated bond strengthening is accounted for by the totally

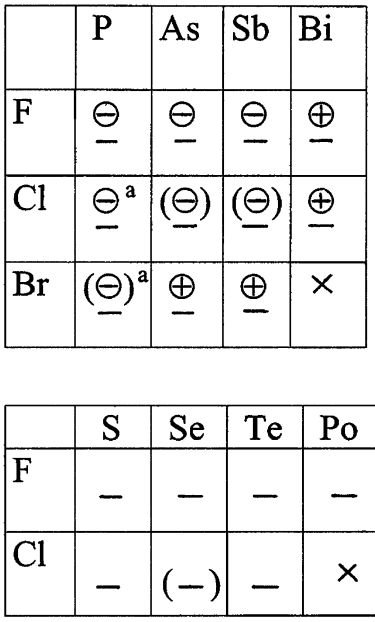

Figure 3. Diagram specifying lone pair distortions with C_{2v} (the superscript a indicates C_s^a; see the text) geometry for complexes $(AX_4^-)_s$ and molecules BX_4 (the iodides in the former case and the bromides and iodides in the latter case are expected by DFT to retain the regular T_d geometry). Signs and circled signs refer to δE_t and $\delta E_t'$ (see eq 6), respectively, indicating whether these energies are positive or negative; signs in parentheses denote $|\delta E_t|$ or $|\delta E_t'|$ energies <0.05 eV and times signs undistorted T_d geometries.

Table 2. Geometrical Data for the C_{2v} (C_s^a) Distorted (Absolute Energy Minima) and the Initial T_d Parent Geometry As Obtained from DFT Geometry Optimizations, for Selected AX_4^- and BX_4 Molecules and Complexes, and in Comparison with Available Structural Data[a]

complex	R_1 (R_1')	R_2	$2\theta_1$	$2\theta_2$	R	ref
$(PF_4^-)_s$ (DFT)	1.80	1.66	189.7	97.5	1.85	
$PF_4^-NMe_4^+$ salt	1.74	1.60	168.3	99.9		23
$(PCl_4^-)_s$ (DFT)	2.57(2.33)	2.11	170.2	101.7	2.32	
$PCl_4^-NMe_4^+$ salt	2.85(2.12)	2.05	171.4	100.0		24
$(PBr_4^-)_s$ (DFT)	2.65(2.60)	2.30	162.6	102.7	2.48	
$PBr_4^-NMe_4^+$ salt	2.62(2.53)	2.24(2)	170.0	99.4		25
SF_4 (DFT)	1.70	1.61	185.0	101.6	1.75	
exptl	1.64	1.54	186.9	100.6		26
SeF_4(DFT)	1.83	1.75	187.6	99.3	1.86	
exptl	1.77	1.68	190.8	100.6		27
SCl_4 (DFT)	2.29	2.08	159.6	103.4	2.21	
$(SCl_4)_s$ (DFT)	2.34	2.04	163.4	103.8	2.22	this work

[a] Angles (deg) and bond lengths (Å) as defined in Figure 1; R = spacings in T_d; $R_1' \neq R_1$ refers to the C_s^a geometry.

(19) Baerends, E. J.; Ellis, D. E.; Ros, P. *Chem. Phys.* **1973**, *2*, 41. Baerends, E. J.; Ros, P. *Int. J. Quantum Chem. Symp.* **1978**, *12*, 169. Baerends, E. J.; Ros, P. *Chem. Phys.* **1973**, *2*, 52. Boerrigter, P. M.; te Velde, G.; Baerends, E. J. *Int. J. Quantum Chem.* **1988**, *33*, 87. te Velde, G.; Baerends, E. J. *J. Comput. Phys.* **1992**, *99*, 84 and references therein. te Velde, G.; Bickelhaupt, F. M.; Baerends, E. J.; Fonesca Guerra, C.; van Gisbergen, S. J. A.; Snijders, J. G.; Ziegler, T. *J. Comput. Chem.* **2001**, *22*, 931.
(20) Klamt, A.; Schüürmann, G. *J. Chem. Soc., Perkin Trans. 2* **1993**, 799.
(21) Pye, C. C.; Ziegler, T. *Theor. Chem. Acc.* **1999**, *101*, 396.
(22) Koch, W.; Holthausen, M. C. *A Chemist's Guide to Density Functional Theory*; Wiley-VCH: Weinheim, New York, 2000; p 87.

Table 3. Energies (eV) of Various Stationary Points in the Ground-State Potential Surface of Selected AX_4^- Complexes and BX_4 Molecules, Imbedded in a Polarizable Solvent Continuum and as Bare Species, As Obtained from DFT Geometry Optimizations

complex		C_{2v}	C_{3v}	*i*-C_{3v}	C_s	C_s^a	C_{4v}
$(PF_4^-)_s$	δE_t	−1.95	−1.21	−1.24	−1.33		−1.52
	$\delta E_t'$	−1.83	−1.17	0.22	−1.06		−1.43
PF_4^-	δE_t	−1.86	−1.19	−0.49	−1.22		−1.45
$(PCl_4^-)_s$	δE_t	−0.57	−0.23	−0.42	−0.45	−0.57	0.11
	$\delta E_t'$	−0.27	−0.11	0.73	0.62	−0.22	0.31
PCl_4^-	δE_t	−0.32	−0.13	−0.03	−0.13		0.30
$(PBr_4^-)_s$	δE_t	−0.26	−0.06	−0.12	−0.14	−0.26	0.45
	$\delta E_t'$	−0.01	0.01	0.72	0.58	−0.01	0.59
PBr_4^-	δE_t	−0.07	−0.01		−0.01		0.60
$(AsF_4^-)_s$	δE_t	−1.00	−0.60	−0.20	−0.61		−0.70
	$\delta E_t'$	−0.73	−0.44	0.04	−0.43		−0.42
AsF_4^-	δE_t	−0.81	−0.50	−0.08	−0.50		−0.52
$(AsCl_4^-)_s$	δE_t	−0.29	−0.10	−0.04	−0.12		0.28
	$\delta E_t'$	−0.01	0.00	0.11	0.06		0.54
$AsCl_4^-$	δE_t	−0.06	−0.01		−0.01		0.52
SF_4	δE_t	−1.93	−1.20	−0.23	−1.22		−1.54
TeF_4	δE_t	−1.03	−0.74	−0.05	−0.74		−0.89
$(SCl_4)_s$	δE_t	−0.33	−0.07	−0.03	−0.12		0.34
	$\delta E_t'$	0.04	0.03	0.41	0.25		0.46
SCl_4	δE_t	−0.09	−0.01		−0.01		0.42

symmetric α_1 stretching mode of the parent tetrahedron. The C_s-type distortion of the P^{III} complexes in Table 2 indicates the presence of τ_2 components of lower symmetry than ζ (Table 1).

III.1.1. AX_4^- Complexes. Let us first consider the halide complexes of the fifth main group with oxidation number III (P to Bi). They are calculated by DFT to adopt distorted (C_{2v} or seldom C_s^a (see below)) geometries (Figure 1) in the case of the fluorides and most of the chlorides and bromides (Figure 3). The iodides and $(BiBr_4^-)_s$ are expected to retain the regular T_d structure, though the potential energy curves along the vibronically active τ_2 modes are flat. The calculated angular and radial distortions in the DFT-optimized C_{2v} geometries are very pronounced (Tables 2 and 4). While the bond angle $2\theta_2$ is close to 100(5)°−10° smaller than the tetrahedral angle—the angle $2\theta_1$ is about 180°, considerably widened with respect to the tetrahedral angle, but may deviate appreciably from linearity by about ±20°. The bond length difference $R_1 - R_2$ is also considerable, increasing from 0.12(2) Å for the fluorides up to about 0.25 Å for the chlorides and bromides, and is even much larger in the cases of $(PCl_4^-)_s$ and $(PBr_4^-)_s$. The diagram in Figure 3 indicates that some complexes are transferred into the distorted geometry just by solvent effects, though there is no electronic lone pair stabilization ($\delta E_t' > 0$, but $\delta E_{solv} + \delta E_t' < 0$)—this occurring because the solvent stabilizes the distorted geometry as the more polar structure considerably stronger than that of the T_d species.

The DFT stabilization energies for the bare complexes[6] agree usually with the $\delta E_t'$ values of the solvated species within 0.1 eV, if the optimized distortion geometries are similar (see Table 3, for example). We further deduce from Table 5, where the enthalpies for the dissociation process with (ΔH_4) and without ($\Delta H_4' = \Delta H_4 - \delta H_4^s$) taking the solvation energy increment δH_4^s into account are collected for some selected complexes, that the solvent stabilizes the X^- anion much more than the larger AX_4^- complex.

$$(AX_4^-)_s \rightarrow AX_3 + (X^-)_s\ (\Delta H_4) \tag{7a}$$

$$AX_4^- \rightarrow AX_3 + X^-\ (\Delta H_4') \tag{7b}$$

Very interesting is the lower-symmetry distortion of $(PCl_4^-)_s$ and $(PBr_4^-)_s$, where the δE_t energy gains are about equal for the $T_d \rightarrow C_{2v}$ and $\rightarrow C_s^a$ pathways (Table 3). The latter is clearly the result of C_{2v} distortions, superimposed by $\tau_2(\xi-\eta)$-type (Figure 1) displacements. It is distinguished from C_{2v} just by (in the $(PCl_4^-)_s$ case considerably) enlarging and reducing either one of the two (longer) bond lengths R_1. There is a further (relative) minimum (saddle point) of C_s symmetry at an only 0.12 eV higher energy, however, where the bond length difference (here, $R_t - R_t'$) is even much larger. While in C_s^a one of the two symmetry planes in C_{2v} is retained, the symmetry plane in C_s has a different orientation (Figure 6). We understand the $C_{2v} \rightarrow C_s^a$ and $C_{2v} \rightarrow C_s$ displacements (see the geometric data in Table 4) as finally aiming at an *i*-C_{3v} geometry, which is very nearby in energy for the two complexes (Table 3). In *i*-C_{3v} (Figure 1) the lone pair is, pictorially speaking, oriented along the *z* direction—repelling one ligand and thus favoring the dissociation process in eqs 7a and 7b (cf. the very long R_t distances of ∼3.5 Å). We think that an *ionic size effect* via the ionic radii ratio $q = r(\text{cation})/r(\text{anion})$—a familiar concept in solid-state chemistry[10]—is present, which drives the geometry from C_{2v} toward *i*-C_{3v}. q is too small for CN = 4 in the cases of the chloride and bromide ligands and initiates the appearance of a minimum at C_s^a and furthermore supports the energy lowering of the stationary points at the C_s and *i*-C_{3v} geometries. The influence of the ionic size effect is also nicely manifested by the magnitudes of the dissociation enthalpies ΔH_4 of $(PBr_4^-)_s$ and in particular $(PCl_4^-)_s$, which are the lowest of all species listed in Table 5. The $(\Delta H_4')^c$ energies in the same table are those enthalpies calculated for eq 7b without taking the vibronic stabilization of AX_4^- and AX_3 from $T_d \rightarrow C_{2v}(C_s^a)$ and from $D_{3h} \rightarrow C_{3v}$, respectively, into account ($(\Delta H_4')^c = \Delta H_4' - (\Delta H_4')^v$). The affiliated vibronic energy increment $(\Delta H_4')^v$ is negative because, according to the hardness rule (see below), a molecule AX_3 undergoes a more pronounced vibronic stabilization than the corresponding AX_4^- complex with higher CN. It is striking that the dissociation energies $(\Delta H_4')^c$ are always smaller for PX_4^- than for the respective AsX_4^- complex, which we take as *energetic* evidence for the presence of an ionic size effect in the case of the smaller P^{III} cation. The latter effect is also reflected by the particularly large vibronic energy increments $(\Delta H_4')^v$ for $(PCl_4^-)_s$ and $(PBr_4^-)_s$; here, the considerable bond length differences between R_1 and R_2 already in C_{2v} reflect a pronounced tendency to reduce the CN. The soft mode nature of the $C_{2v} \rightarrow C_s^a$ transition may explain why the DFT-calculated bond length differences ($R_1 - R_1'$) deviate considerably from the experimental ones; there is obviously a high sensitivity of the flat potential curve following the C_{2v} (C_s^a) → *i*-C_{3v} pathway with respect to the polarity of the specific chemical

Table 4. Bond distances (Å) and bond Angles (deg) for Stationary Points with Lower (Than T_d) Symmetry for CN = 4 Species with an s^2 Lone Pair, As Obtained from DFT Geometry Optimizations[a]

	C_{2v}			C_{3v}			C_s			i-C_{3v}			C_{4v}	
complex	R_1 R_2	$2\theta_1$ $2\theta_2$	θ_{12}	R_t R_t'	θ_t	α_t	R_t R_t'	θ_t	α_t	R_t R_t'	θ_t	α_t	R	θ
$(PF_4^-)_s$	1.80	189.7	86.8	1.67			1.65			3.31			1.74	111.8
	1.66	97.5		1.79	83.9	118.9	1.70 (2×)	89.4 (2×)	96.0	1.62	120.6	96.4		
							2.09	79.7	131.0 (2×)					
$(AsF_4^-)_s$	1.94	190.6	86.5	1.81			1.80			2.28			1.88	113.2
	1.81	96.4		1.93	84.0	118.9	1.89 (2×)	86.0 (2×)	101.2	1.84	122.6	93.7		
							2.01	82.2	128.0 (2×)					
$(AsCl_4^-)_s$	2.51	169.0	93.6	2.26			2.25			2.66			2.39	108.1
	2.25	99.3		2.44	94.7	119.3	2.37 (2×)	96.0 (2×)	103.9	2.32	116.9	101.1		
							2.60	92.7	127.0 (2×)					
SF_4	1.69	185.0	88.4	1.61			1.61			1.89			1.66	109.2
	1.60	100.4		1.71	86.0	119.5	1.68 (2×)	87.5 (2×)	103.6	1.68	121.6	95.0		
							1.74	84.4	127.6 (2×)					
TeF_4	1.97	193.5	85.7	1.90			1.90			2.06			1.94	112.6
	1.91	100.0		1.97	83.5	118.7	1.97 (2×)	83.5 (2×)	118.0	1.97	119.8	97.4		
							1.97	83.4	119.1 (2×)					
SCl_4	2.29	159.6	96.3	2.10			2.11			2.22			2.19	104.2
	2.08	103.4		2.24	100.7	116.6	2.24 (2×)	101.1 (2×)	115.6	2.21	110.0	108.9		
							2.25	101.1	116.7 (2×)					
$(SCl_4)_s$	2.34	163.4	95.1	2.05			2.05			2.56			2.20	104.9
	2.04	103.8		2.26	98.3	118.0	2.17 (2×)	100.4 (2×)	105.6	2.12	114.5	104.0		
							2.48	95.6	123.8 (2×)					

	C_{2v}			C_s[a]			C_{3v}			C_s			i-C_{3v}			C_{4v}	
complex	R_1 R_2	$2\theta_1$ $2\theta_2$	θ_{12}	R_1 (R_1') R_2	$2\theta_1$ $2\theta_2$	θ_{12}	R_t R_t'	θ_t	α_t	R_t R_t'	θ_t	α_t	R_t R_t'	θ_t	α_t	R	θ
$(PCl_4^-)_s$	2.44	170.6	93.0	2.57 (2.33)	170.2	91.7 (2×)	2.10			3.37			3.57			2.28	107.4
	2.11	101.4		2.11	101.3	94.5 (2×)	2.36	94.2	119.5	2.12 (2×)	128.5 (2×)	100.6	2.10	117.2	100.7		
										2.10	86.6	100.1 (2×)					
$(PBr_4^-)_s$	2.62	162.5	95.5	2.65 (2.60)	162.6	95.2 (2×)	2.30			3.23			3.39			2.47	106.0
	2.30	102.0		2.30	102.1	95.7 (2×)	2.53	98.5	117.8	2.32 (2×)	126.0 (2×)	101.9	2.30	116.3	101		
										2.29	93.4	101.0 (2×)					

[a] Bond lengths R_1, R_1', R_2, R_t, and R_t' and bond angles $2\theta_1$, $2\theta_2$, θ_t and α_t are defined in Figure 1 (θ_{12} (4×) are the remaining angles in C_{2v}; $R_1 = R_2 = R$ and $2\theta_1 = 2\theta_2 = \theta$ refer to C_{4v}). The geometric data for C_s in the upper part of the table refer to the C_{3v} setting (trigonal compression), and those for $(PCl_4^-)_s$ and $(PBr_4^-)_s$ refer to i-C_{3v} (trigonal elongation); the C_s^a setting is that of C_{2v} (see the text).

Table 5. Dissociation Enthalpies (eV) ΔH_4, Solvation Energies δH_4^s, and the $\Delta H_4'$ Enthalpy Increments $(\Delta H_4')^c$ and $(\Delta H_4')^v$ for Selected Complexes AX_4^- (A = P, As; X = F, Cl, Br), $\Delta H_4 = \Delta H_4' + \delta H_4^s$, $\Delta H_4' = (\Delta H_4')^c + (\Delta H_4')^v$

	P, F	As, F	P, Cl	As, Cl	P, Br	As, Br
$(\Delta H_4')^c$	3.56	4.18	3.00	3.17	2.75	2.87
$(\Delta H_4')^v$	−1.04	−1.28	−1.64	−1.42	−1.48	−1.26
δH_4^s	−1.92	−1.77	−1.22	−1.25	−1.05	−1.13
ΔH_4	0.60	1.13	0.14	0.50	0.22	0.48

environment. We finally emphasize that the "anomalous" $C_{2v} \rightarrow C_s^a$ distortion occurs only due to the support by the solvent.

Tables 3 and 4 survey the vibronic landscape of selected complexes $(AX_4^-)_s$ and some BX_4 molecules, with its various extremum points corresponding to energies which are fully optimized with the constraint of the respective point group. One first notes that a C_s^a stationary point only exists for the chloro and bromo complexes of P^{III}; otherwise there is no pronounced tendency to repel one ligand toward a particularly long bond distance. The $(AsX_4^-)_s$ (X = F, Cl) polyhedra with C_s symmetry are geometrically closely related to those of the compressed C_{3v} type, and the respective C_s and C_{3v} minima are close in energy; in contrast, the i-C_{3v}-distorted polyhedra lie at distinctly higher energies (Tables 3 and 4; $(PF_4^-)_s$, with about equal C_{3v} and i-C_{3v} energies, represents an intermediate case).

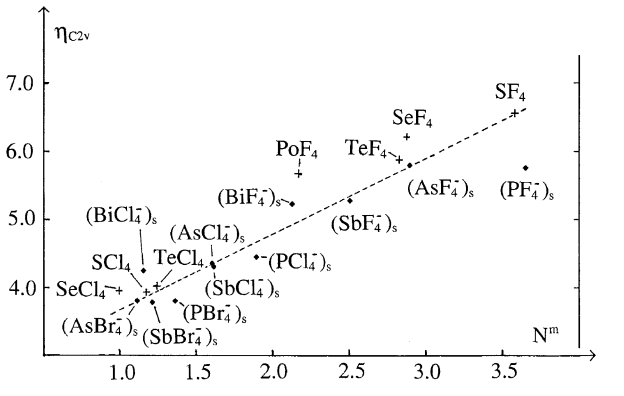

Figure 4. Energy plot (eV) of the chemical hardness $\eta(C_{2v})$ versus N^m—representing the lone pair activity—for complexes $(AX_4^-)_s$ and molecules BX_4.

In Figure 4 we show the dependence of the chemical hardness $\eta_{C_{2v}}$ on the vibronic coupling energy N^m. The complexes become softer and hence more susceptible to lone pair effects if one moves from the fluorides to the chlorides and finally to the bromides; a much less pronounced gradation is observed on proceeding from P^{III} to Bi^{III}. In the case of the iodides a still finite fictive N^m value can be suggested; however, because E_{vib}^m is not large enough anymore to overcome E_{rf}^m (eq 3), it bears no reality. This argument will be taken up below again. The large deviation

Table 6. Vibronic Parameters (eV; See the Text for Definitions) of the PJT Interaction in Tetrahedral $(AX_4^-)_s$ Complexes and BX_4 Molecules Possessing an s^2 Lone Pair, for the C_{2v} (C_s^a) Ground-State Minimum[a]

complex	δE_t	$\delta E_t'$	E_{vib}^m	E_{rf}^m	E_{FC}^m	N^m	$\eta_{C_{2v}}$	η_{T_d}
$(PF_4^-)_s$[b]	−1.94	−1.83	2.49	0.66	7.84	3.65	5.76	5.27
$(AsF_4^-)_s$	−1.00	−0.73	1.61	0.88	6.79	2.89	5.80	5.49
$(SbF_4^-)_s$	−0.93	−0.54	1.17	0.63	6.51	2.50	5.28	5.09
$(BiF_4^-)_s$	−0.30	0.24	0.86	1.10	6.08	2.12	5.23	5.33
$(PCl_4^-)_s$	−0.57	−0.27	1.24	0.97	4.12	1.89	4.45	4.08
$(AsCl_4^-)_s$	−0.30	−0.01	0.81	0.80	4.00	1.60	4.36	4.26
$(SbCl_4^-)_s$	−0.37	−0.04	0.78	0.74	4.09	1.61	4.31	4.11
$(BiCl_4^-)_s$	−0.07	0.20	0.36	0.56	4.06	1.15	4.25	4.37
$(PBr_4^-)_s$	−0.26	−0.01	0.72	0.71	3.30	1.36	3.81	3.68
$(AsBr_4^-)_s$	−0.10	0.11	0.43	0.54	3.26	1.11	3.81	3.83
$(SbBr_4^-)_s$	−0.22	0.06	0.51	0.57	3.40	1.21	3.79	3.73
SF_4	−1.93		2.74	0.81	7.42	3.58	6.56	5.56
SeF_4	−1.04		1.74	0.70	6.47	2.87	6.22	5.66
TeF_4	−1.03		1.69	0.66	6.41	2.82	5.88	5.42
PoF_4	−0.14		1.27	1.13	5.94	2.44	5.98	5.75
SCl_4	−0.09		0.67	0.58	2.72	1.17	3.94	3.89
$SeCl_4$	−0.01		0.41	0.40	2.80	0.99	3.96	4.03
$TeCl_4$	−0.17		0.60	0.43	3.15	1.24	4.03	3.94
$(SBr_4)_s$	−0.04	0.22	0.32	0.54	2.25	0.78	3.38	3.52
$(TeBr_4)_s$	−0.09	0.08	0.36	0.44	2.57	0.90	3.44	3.55

[a] The chemical hardness η in C_{2v} and in the T_d parent geometry is also listed. [b] Double-ζ basis.

of $(PF_4^-)_s$ from the linear dependence is due to an unexpectedly small C value (eq 5b and the Appendix). Though the strong coupling approximation ($E_{FC}^m \cong 2N^m$) does not hold for complexes with N^m energies below 1.5 eV anymore, the linear correlation is still fairly good. When the results in Figure 4 and Table 6 are compared with those for the AX_3 molecules,[5,6] it is striking that the η and N^m values are always distinctly smaller for an $(AX_4^-)_s$ complex than for the corresponding AX_3 molecule: *Increasing the coordination number leads to a softening of the complex or molecule and hence to a decreased readiness for lone pair distortions*. The anionic charge does not seem to alter the vibronic coupling energy significantly, because model calculations on $(PF_4^-)_{solv}$ and SF_4–removing an electron from the nonbonding a_2 MO in the C_{2v} distorted geometry (see the MO scheme in Figure 5)—show that the resulting species $(PF_4)^*_{solv}$ and $(SF_4^+)^*_{solv}$ possess nearly the same vibronic coupling energies N^m and E_{vib}^m as those of the original entities.

If we regard the anomalous geometry of in particular the $(PCl_4^-)_s$ complex as a C_{2v} deformation, perturbed by a $\tau_2(\xi-\eta)$-type distortion component (see section II.2 and Figure 1), we find that the small $\delta E_t'$ increase from C_{2v} to C_s^a (0.05 eV) is mainly a restoring energy effect ($\delta E_{rf}^m \cong 0.07$ eV; $\delta E_{vib}^m \cong 0.02$ eV). There is obviously only a weak resistance (see the tiny ($\delta E_{rf}^m + \delta E_{solv}$) energy of 0.02 eV) toward removing one ligand from the coordination sphere—in agreement with the DFT-suggested soft mode behavior.

III.1.2. BX_4 Molecules. We now turn to the discussion of the BX_4 molecules. The 12 tetrahalides of Se, Te, and Po are known (except perhaps SeI_4) as liquids (SeF_4) or solids[1]—in which due to interconnections between the polyhedra the CN is larger than 4—while from sulfur only SF_4 and SCl_4 have been prepared. According to DFT only the fluorides and chlorides with the exception of $PoCl_4$ are calculated to possess lowest energy minina at C_{2v} geometry (Figure 3), with again two nearly linear ($2\theta_1$ between 160° and 190°) and longer bonds (R_1) and two shorter bonds (R_2) contending an angle $2\theta_2$ of about 100° (Figure 1); the other BX_4 molecules should be of regular tetrahedral geometry. SF_4 and SeF_4 have been structurally characterized as gas-phase species by microwave spectroscopy (Table 2).

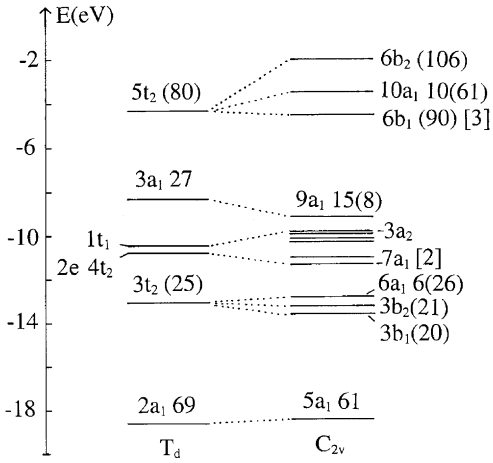

Figure 5. Kohn−Sham MO energy diagram of TeF_4 for DFT-optimized T_d and C_{2v} geometries with the tellurium 5s and 5p (in parentheses) and 5d (in brackets) electron density contributions. The symmetry-adapted LCAOs in T_d originating from the ligand 2s and 2p AOs are $a_1(\sigma)$, $t_2(\sigma)$ and $a_1(\sigma)$, $t_2(\sigma+\pi)$, respectively, as well as e, t_1, and t_2 (nonbonding); the Te(5s,5p) AOs commute to $a_1(\sigma)$ and $t_2(\sigma+\pi)$. The T_d MOs transform in C_{2v} as follows: e → a_1, a_2; t_1 → a_2, b_1, b_2; t_2 → $a_1(||z)$, $b_1(||x)$, $b_2(||y)$. The only weakly bonding $1a_1$ and $1t_2$ MOs from 2s (F) at ∼−28.5 eV are not shown; the C_{2v} split components of the nonbonding MOs are only partly depicted.

In Figure 5 we depict the MO diagram for TeF_4, which illustrates the energetic effects underlying the structural distortion. The shortening of the average Te−F bond from 2.00 (T_d) to 1.94 Å (Table 4) leads to an increase in energy of the antibonding $3a_1$ HOMO and $5t_2$ LUMO and of most of the other MOs, thus diminishing the total bonding energy—if the system would remain in T_d (this effect is not shown separately in the diagram). This unfavorable energy change is largely overcompensated by that due to the symmetry-breaking distortions. The Jahn−Teller mode $\epsilon(\theta)$ induces in particular a strong repulsion between the HOMO and the z component $10a_1$ of the LUMO, thus creating an MO sequence where $6b_1$ is found at a lower energy than

$10a_1$. The total $T_d \rightarrow C_{2v}$ energy change $\delta E_t = E_-{}^m = -1.03$ eV is predominantly reflected by the stabilization of the electron pair in the HOMO (-2×0.80 eV).

The DFT decomposition of δE_t into δE_P, δE_{el}, and δE_{orb}—with a further subdivision of the latter, where the component $\delta E_{orb}(a_1)$ comprises among others the total orbital energy change induced by the vibronic process—provides further insight into the origin of the instability. δE_P and δE_{el} are completely (or nearly completely) contained in the restoring energy $E_{rf}{}^m$, while $E_{vib}{}^m$ is a purely (or at least predominantly) orbital effect and dominated by $\delta E_{orb}(a_1)$. δE_P does not favor the distortion process as stated by VSEPR;[4] instead it increases—only slightly due to $\tau_2(\zeta)$ and $\epsilon(\theta)$ but dramatically due to α_1. While $E_{rf}{}^m$ is usually a positive energy (Tables 6 and 10), this is not necessarily so. DFT calculations suggest that some of the softer AX_3 molecules should undergo spontaneous distortions $D_{3h} \rightarrow C_{3v}$ already without vibronic coupling.[7] The restoring energy $|E_{rf}{}^m|$ is small with respect to the dominating $E_{vib}{}^m$ contribution in these cases, however (for example, $SbBr_3$, $E_{rf}{}^m = -0.18$, $E_{vib}{}^m = 0.95$, $\delta E_t = -1.13$ eV).[28]

In Figure 4 we show the $\eta_{C_{2v}}/N^m$ correlation for the BX_4 molecules, in addition to that for the $(AX_4^-)_s$ complexes. Again the essentials of the hardness rule are distinctly recognizable; the molecules become softer and less easily accessible to lone pair distortions, if X^- is changed from fluoride to chloride—with a smaller effect on moving from S^{IV} to Po^{IV} in the case of the fluorides. The comparison between the BX_4 molecules and the respective isoelectronic $(AX_4^-)_s$ complexes is not completely obvious, however. While for the fluorides the former have distinctly larger hardness values $\eta_{C_{2v}}$, with comparable N^m vibronic coupling energies for both groups, in the case of the chlorides and bromides the $(AX_4^-)_s$ species range distinctly higher in the hardness sequence than corresponding BX_4 molecules (Table 6). Thus, we can only very roughly correlate elements from the fifth main group (A^{III}) with those from the sixth main group (B^{IV}) with respect to their lone pair activities. A critical remark is necessary here. Equation 5 relates the chemical hardness to the Franck–Condon energy between the many-electron A_1 states in C_{2v} as the result of the vibronic interaction between $A_1(...s^2)$ and the p_z component of $T_2(...s^1p_z^1)$ in T_d (see the $3a_1$ HOMO and $5t_2$ LUMO in Figure 5). However, for the distorted BF_4 molecules the chemical hardness $\eta_{C_{2v}}$ is a property which involves the a_1 MO housing the lone pair and the LUMO b_1, which is the first excited state in these cases instead of a_1. Thus, the hardness for these molecules can be significantly smaller than that which is the basis of eq 5; for SF_4 this discrepancy is considerable, 6.56 eV instead of 7.38 eV, while for PoF_4 the effect is already negligible, 5.68 eV instead of 5.82 eV. A small effect is also recognizable in the case of $(AsF_4^-)_s$, for example, with $\eta_{C_{2v}} = 5.80$ eV instead of 6.02 eV. Despite this disturbance, the hardness rule still works fairly well.

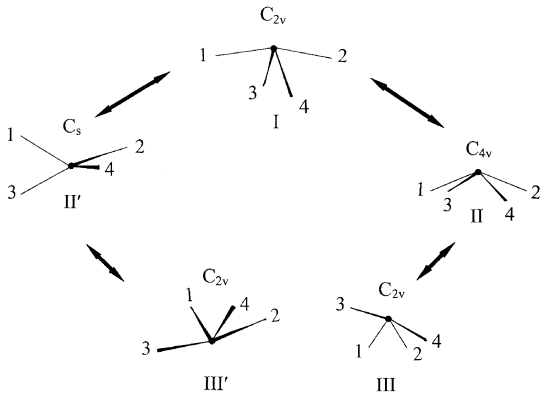

Figure 6. Fluxionality of C_{2v}-distorted tetrahedra: (a) C_{2v} (I) $\rightarrow$ C_{2v} (III) via a C_{4v} transition state (II), Berry-type mechanism (1,2 to 3,4 ligand interchange); (b) C_{2v} (I) $\rightarrow$ C_{2v} (III′) via a C_s transition state (II′), lever mechanism (1 to 3 ligand interchange).

It was mentioned above that—in a fictive sense—finite N^m values may exist also for complexes and molecules which are electronically stable against distortions, because $E_{vib}{}^m$ is smaller than $E_{rf}{}^m$. Convincing proof for this suggestion is the molecules SBr_4 and $TeBr_4$, which are expected to appear as undistorted tetrahedra in the bare state (Figure 3), but adopt a C_{2v} geometry, when surrounded by a solvent continuum. The interactions with the polarizable solvent stabilize the distorted geometry more than the T_d parent geometry; thus, the δE_{solv} contribution induces a negative δE_t in these cases (Table 6). Since the electronic parameters on the other hand are not significantly altered by the solvent continuum, the listed vibronic energies for $(SBr_4)_s$ and $(TeBr_4)_s$ represent in good approximation also those which would characterize the bare molecules in the distorted geometry.

Within the multidimensional potential energy surface describing the vibronic interaction in T_d, there is a rich variety of stationary points (characterized by zero energy gradients) which may give insight into the dynamics of tautoisomerization. Thus, it has been observed for SF_4 by NMR spectroscopy[29] that the ligand pairs 1 and 2, and 3 and 4 in Figure 6 undergo rapid interchange above ~225 K. The transition state II between the two conformations I and III possesses C_{4v} symmetry within the error limit (Tables 3 and 4). The activation energy for the fluxionality process is calculated to amount to $\Delta E_a = \delta E_t(C_{4v}) - \delta E_t(C_{2v}) = 0.39$ eV. This barrier is distinctly smaller than that for an exchange of ligand 1 (or 2) with ligand 3 (or 4), where C_s stationary points II′ would represent the transition state ($\Delta E_a = 0.71$ eV). This is different, however, on proceeding to SCl_4 and $TeCl_4$ with the bulkier Cl ligands. Here, a C_s-type (lever) mechanism ($\Delta E_a \approx 0.1$ eV), rather than a C_{4v} (Berry) pseudorotation ($\Delta E_a \approx 0.5$ eV (SCl_4) and 0.25 eV ($TeCl_4$)),

(23) Christe, K. O.; Dixon, D. A.; Mercier, H. P. A.; Sanders, J. C. P.; Schrobilgen, G. J.; Wilson, W. W. *J. Am. Chem. Soc.* **1994**, *116*, 2850.
(24) Dillon, K. B.; Platt, A. W. G.; Schmidpeter, A.; Zwaschka, F.; Sheldrick, W. S. *Z. Anorg. Allg. Chem.* **1982**, *488*, 7.
(25) Sheldrick, W. S.; Schmidpeter, A.; Zwaschka, F.; Dillon, K. B.; Platt, A. W. G.; Waddington, T. C. *J. Chem. Soc., Dalton Trans.* **1981**, 413.
(26) Kimura, K.; Bauer, S. H. *J. Chem. Phys.* **1963**, *39*, 3172.
(27) Seppelt, K. *Z. Anorg. Allg. Chem.* **1975**, *416*, 12. Damerius, R.; Huppmann, P.; Lentz, D.; Seppelt, K. *J. Chem. Soc., Dalton Trans.* **1989**, 2821.
(28) Reinen, D.; Atanasov, M. *Struct. Bonding (Berlin)*, Vol. 107, **2004**.
(29) Seel, F.; Gombler, W. J. *J. Fluorine Chem.* **1974**, *4*, 327. Klemperer, W. G.; Krieger, J. K.; McCreary, M. D.; Muetterties, E. L.; Traficante, D. D.; Whitesides, G. M. *J. Am. Chem. Soc.* **1975**, *97*, 7023.

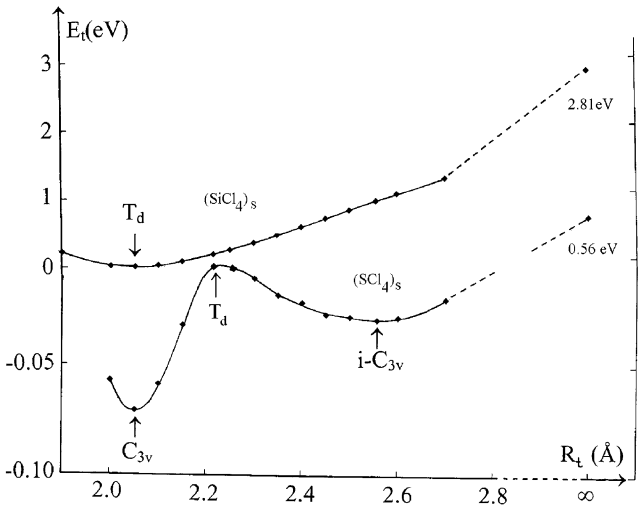

Figure 7. Total energy changes δE_t (Table 3) of the $(SCl_4)_s$ tetrahedron along the $T_d \rightarrow i\text{-}C_{3v}$ and $\rightarrow C_{3v}$ displacement paths in dependence on the long ($i\text{-}C_{3v}$) and short (C_{3v}) S−Cl spacing R_t, respectively (see Figure 1). Every energy is optimized with respect to the other S−Cl spacings and all Cl−S−Cl angles. For comparative purposes the energy changes for the tetrahedral $(SiCl_4)_s$ molecule without the lone pair are included. Stationary points—relative minima at C_{3v} and $i\text{-}C_{3v}$ and the energies for the complete dissociation of one ligand—are indicated.

is expected to operate. For the PF_4^- complex in frozen solution the same pseudorotation as for SF_4 is reported, in perfect agreement with the energy landscape in Table 3. The calculated energy barrier via the C_{4v} transition state (0.43 eV) is exactly the experimental value.[23] We note (see Figures 1 and 6) that—within the lever mechanism—there is no direct transition from C_{2v} (I) to C_s (II'), because the mirror plane in C_s contains ligands 1 and 3, while that in C_{2v} is correlated with ligands 1 and 2 (C_{2v} (I) $\rightarrow C_1 \rightarrow C_s \rightarrow C_1 \rightarrow C_{2v}$ (III'), interchange of one ligand at R_1 with one at R_2).

Literature reports about the tendency of the BX_4 chlorides and bromides toward the formation of BX_3^+ cations, such as $SeBr_3^+$ and $TeCl_3^+$, in the presence of halide ion acceptors (Lewis acids) such as $GaCl_3$, $AlCl_3$, $AlBr_3$, or AX_5 (A = As, Sb; X = F, Cl).[30,31] Furthermore, SCl_4 can only be obtained as a stable compound the in form of an "adduct", $SCl_4 \cdot AlCl_3$, which is better formulated as $SCl_3^+AlCl_4^-$. We have studied this property by DFT, analyzing more closely the C_{3v} and $i\text{-}C_{3v}$ distortion pathways (Tables 2 and 3). Figure 7 displays the energies of these pathways for $(SCl_4)_s$ in dependence on the S−Cl bond length along the C_3 axis. Here, C_{3v} refers to displacements of the ligand on the z axis according to a shrinking of the respective B−X bond length, while $i\text{-}C_{3v}$ is correlated with an increase of this spacing—orientation of the lone pair $||(-z)$ and $||z$, respectively (Figure 1). Relative minima (saddle points in full configurational space) are observed with δE_t energies <0, which are higher by 0.26 eV (C_{3v}) and 0.30 eV ($i\text{-}C_{3v}$) than the absolute C_{2v} energy minimum (Table 3). Also, the dissociation enthalpy for the process $(SCl_4)_s \rightarrow (SCl_3^+)_s + (Cl^-)_s$ is rather small (0.56 eV with respect to the C_{2v} distorted molecule)—obviously due to a stabilizing contribution from the vibronic coupling along the $i\text{-}C_{3v}$ pathway, which becomes immediately clear when $(SCl_4)_s$ is compared with $(SiCl_4)_s$ lacking the lone pair. In the latter case a considerably larger dissociation enthalpy is afforded (2.81 eV with respect to T_d). We readily conclude that the tendency of many BX_4 molecules to form $BX_3^+X^-$ species is strongly promoted by vibronic interactions—in contrast to the corresponding $B'X_4$ molecules without the lone pair. A supporting ionic size effect as discussed for $(PCl(Br)_4^-)_s$ cannot be detected. This observation is somewhat surprising, because the ionic radius of S^{IV} is smaller than that of P^{III}. Obviously electrostatic considerations cannot be applied here anymore, because the S^{IV}−Cl bond is expected to be strongly covalent already—in contrast to the P^{III}−Cl bond in $(PCl_4^-)_s$.

Table 7. Geometric Data (Bond Lengths, Å; Bond Angles, deg) for Selected AX_5^{2-}, BX_5^-, and CX_5 Species in the D_{3h} Parent (R_{ax}, R_{eq}) and the C_{2v} (=C_{4v}) Final Geometry ($R_{eq} \rightarrow R_{ap}$, R_b^1 and $R_{ax} \rightarrow R_b^2$, with $R_b^1 = R_b^2 = R_b$ and $\theta = \varphi$ in C_{4v}; See Figure 2), DFT-Calculated in Comparison with Experimental Values

	D_{3h}		C_{4v}			
model complex	R_{ax}	R_{eq}	R_{ap}	R_b	θ	ref
$(SbCl_5^{2-})_s$ (DFT)	2.68	2.64	2.46	2.68	90.2	
$(SbF_5^{2-})_s$ (DFT)	2.18	2.17	2.02	2.13	80.8	
SbF_5^{2-} in K^+ salt			2.00	2.04	83.0	32
$(SF_5^-)_s$ (DFT)	1.82	1.84	1.64	1.79	86.0	
SF_5^- in NMe_4^+ salt			1.56	1.72	85.0	33
in Rb^+ salt			1.56	1.72	85.0	
$(SeF_5^-)_s$ (DFT)	1.93	1.93	1.79	1.90	85.0	
SeF_5^- in NMe_4^+ salt			1.71	1.85	84.0	34
$(TeF_5^-)_s$ (DFT)	2.07	2.07	1.94	2.03	81.8	
TeF_5^- in NMe_4^+ salt			1.84	1.96	81.0	34
ClF_5 (DFT)	1.76	1.80	1.68	1.74	87.6	
ClF_5 gaseous			1.62	1.72	~90.0	1
BrF_5 (DFT)	1.86	1.88	1.79	1.84	86.7	
BrF_5 gaseous			1.69	1.77	84.8	1
IF_5 (DFT)	1.99	2.00	1.90	1.95	83.7	
IF_5 gaseous			1.84	1.87	81.9	1

III.2. Coordination Number 5. The vibronic calculations for all investigated molecules and solvated complexes yield that the C_{2v} distortion pathway is mostly energetically preferred; somewhat surprisingly it always leads to an apparent C_{4v} geometry (Figure 2, $R_b^1 = R_b^2$, $\varphi = \theta$). In Table 7 calculated geometries of some species are compared with available experimental structural data. There is essential agreement between these results, though the calculated bond lengths are again (see section III.1) larger—here by about 4%. We also note that—as was discussed in the CN = 4 case already—the steric transition from D_{3h} to C_{4v} geometry is always accompanied by a significant decrease of the average bond length, which amounts to 0.05(2) Å in the cases selected in Table 7. In an electrostatic description this means that the ionic radius of a lone pair cation in the high-symmetry parent polyhedron is generally significantly larger, due to the repulsive force of the spherically symmetric s^2 pair, than—when the bond lengths are averaged—that in the distorted geometry.

(30) Christian, B. H.; Collins, M. J.; Gillespie, R. J.; Sawyer, J. F. *Inorg. Chem.* **1986**, *25*, 777.
(31) Beck, J.; Schlörb, T. *Z. Kristallogr.* **1999**, *214*, 780.
(32) Byström, A.; Wilhelmi, K. A. *Arkiv Kemi* **1951**, *3*, 461. Mastin, S. H.; Ryan, R. R.; Asprey, L. B. *Inorg. Chem.* **1970**, *9*, 2100.
(33) Mahjoub, A. R.; Seppelt, K. *Angew. Chem.* **1991**, *103*, 309; *Angew. Chem., Int. Ed. Engl.* **1991**, *30*, 323.
(34) Mahjoub, A. R.; Leopold, D.; Seppelt, K. *Z. Anorg. Allg. Chem.* **1992**, *618*, 83.

	P	As	Sb	Bi
F	⊖ —	⊖ —	⊖ —	⊕ —
Cl	⊖ [a] —	⊕ —	⊕ —	⊕ —
Br	(⊖) —	⊕ —	⊕ —	⊕ (−)
I	×	⊕ —	⊕ (−)	⊕ (±)

	S	Se	Te
F	⊖ —	⊖ —	⊖ —
Cl	(⊖) —	⊕ —	(⊖) —
Br	⊕ —	⊕ (−)	⊕ —

Figure 8. Diagram specifying lone pair distortions with a C_{2v} (C_{4v}) (the superscript a indicates C_s; see the text) geometry for complexes $(AX_5^{2-})_s$ and $(BX_5^{-})_s$. Signs and circled signs refer to δE_t and $\delta E_t'$ (see eq 6), respectively, indicating whether these energies are positive or negative; signs in parentheses denote $|\delta E_t|$ or $|\delta E_t'|$ energies <0.05 eV (×, undistorted D_{3h} geometry; ±, vanishing energy).

III.2.1. $(AX_5^{2-})_s$ Complexes. Figure 8 illustrates that only the smaller part of the charge-compensated complexes is electronically stabilized ($\delta E_t' < 0$) by distortion from D_{3h} to C_{2v} ($\cong C_{4v}$); there are even fewer examples with $\delta E_t' < 0$ than in the CN = 4 case (Figure 3). Most of the remaining polyhedra are expected to also distort, but only due to a negative solvent contribution which surpasses the positive $\delta E_t'$ value (eq 6). DFT calculations on the bare anions have already been performed,[6] which essentially agree with the schematic diagram in Figure 8 if only the electronic stabilization $\delta E_t'$ is considered—as expected. The total stabilization energy $|\delta E_t|$ is ≤0.15 eV or even vanishing in these cases, indicating flat potential curves along the nuclear displacement paths of the vibronically active modes. The calculated bond length differences between $R_b^1 = R_b^2$ and R_{ap} in C_{4v} vary between 0.12 Å $(BiF_5^{2-})_s$ and 0.31 Å $(PBr_5^{2-})_s$, while the bond angle 2θ is about 166(3)° for the fluorides and 188(6)° for the chlorides and bromides. $(PCl_5^{2-})_s$ is unusual concerning the nature of the distortion. Superimposed on a very large C_{2v} (=C_{4v}) deformation we

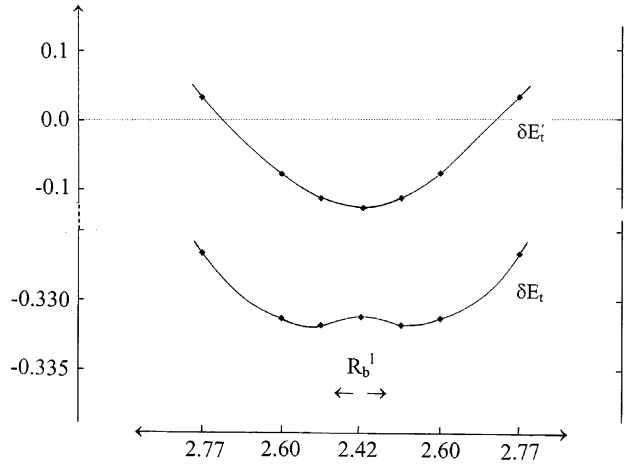

Figure 9. Total energy changes (δE_t, eV) of the $(PCl_5^{2-})_s$ complex along the $C_{2v}(C_{4v}) \rightarrow C_s$ distortion path in dependence on the P−Cl spacing (Å) $R_b^1 \rightarrow R_b^1$ (Figure 2). The energy changes $\delta E_t'$ without including the solvent energy are also shown. Every energy is optimized with respect to all other P−Cl spacings and Cl−P−Cl angles.

calculate by DFT additional displacements of $\epsilon'_s(\zeta)$ and $\epsilon'_{ip}(\zeta)$ type, which operate along the two R_b^1 bond lengths and via the φ angle. The resulting C_s distortion is distinguished from C_{4v} mainly by enlarging one of the R_b^1 spacings (R_b^l) and reducing the other one (R_b^s) (see Figure 2 and Table 8). Similar to the C_s^a distortion away from C_{2v} in the tetrahedral case, also here the energetic reason is a pronounced tendency to lower the CN from 5 to 4. The involved displacement path aims at an $(i\text{-}C_{2v})'$ geometry, which is distinguished from the symmetry-equivalent C_{2v} distorted polyhedron in that it involves the R_b^l bond length as the preferred axis instead of R_{ap}. The geometric situation near the dissociation limit would be a butterfly-shaped tetrahedron with a long-distance-bonded fifth ligand along R_b^l—the lone pair direction. Figure 9 illustrates that it is again the solvent contribution which finally stabilizes $(PCl_5^{2-})_s$ in the very shallow minimum at C_s geometry. Though all other complexes and molecules with CN = 5 investigated here are calculated to have their stable minima at the $C_{2v} \approx C_{4v}$ geometry, a soft mode behavior along the considered C_s distortion path is found for many of these according to DFT, in particular for the $(PX_5^{2-})_s$ complexes. The $i\text{-}C_{2v}$ distortion path (elongation of R_{ap}; see Figure 2) is, as expected, energetically distinctly discriminated against ligand displacements following the $\epsilon'_s(\zeta)$ and $\epsilon'_{ip}(\zeta)$ modes via C_s toward $(i\text{-}C_{2v})'$. Whenever a tendency toward the ablation of one ligand exists, the latter path will be chosen.

Though the correlation in the $\eta_{C_{2v}}$ versus N^m diagram (Figure 10a) is quantitatively not too good—mostly due to

Table 8. C_{4v} and C_s Geometries (Bond Lengths, Å; Bond Angles, deg) of the $(PCl_5^{2-})_s$ and $(SeCl_5^{-})_s$ Complexes (Calculated) and of $SeCl_5^-$ in $[PCl_4]SeCl_5$[35]

	C_{4v}			C_s					
complex	R_{ap}	R_b	$\theta = \varphi$	R_{ap}	R_b^l	R_b^s	R_b^2	θ	φ
$(PCl_5^{2-})_s$ (DFT)	2.13	2.46	93.5	2.13	2.51	2.41	2.46	93.5	93.0 (R_b^l) 94.2 (R_b^s)
$(SeCl_5^{-})_s$ (DFT)	2.23	2.43	95.0	2.19	2.49	2.30	2.38	88.5	89.4 (R_b^1)
$PCl_4^+SeCl_5^-$									94.9 (R_b^s)

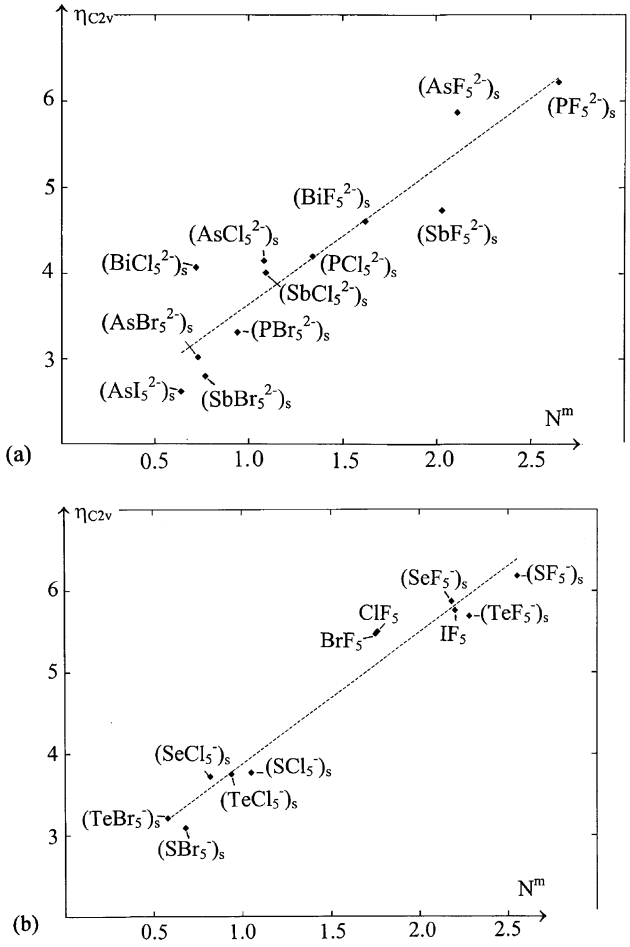

Figure 10. Energy plot (eV) of the chemical hardness $\eta(C_{2v})$ versus N^m—representing the lone pair activity—for (a, top) complexes $(AX_5^{2-})_s$ and (b, bottom) complexes $(BX_5^-)_s$ and CF_5 molecules.

the failure of the strong vibronic coupling approximation in most cases (eq 5b)—it still demonstrates very nicely the validity of the hardness rule: the softer the ligands (from F^- to I^-) and (less pronounced) the central ions (from P^{III} to Bi^{III}), the more the complexes resist lone pair distortions.

The enthalpies (Table 9) for the dissociation processes

$$(AX_5^{2-})_s \rightarrow (AX_4^-)_s + (X^-)_s \; (\Delta H_5) \qquad (8a)$$

$$AX_5^{2-} \rightarrow AX_4^- + X^- \; (\Delta H_5') \qquad (8b)$$

indicate—contrasting the results for CN = 4 (eqs 7a and 7b)—that the solvent strongly stabilizes the five-coordinate species ($\delta H_5^s > 0$), because the doubly charged anion undergoes much larger electrostatic interactions than the two singly charged species. This solvent effect is even larger, when complexes with CN = 6 are considered.[6] The $(\Delta H_5')^c$ energy increments of the P^{III} complexes suggest a more pronounced attitude toward dissociation than those of the corresponding As^{III} complexes. We think that an ionic-size-type instability is responsible again, which—in contrast to CN = 4 (Table 5)—also strongly affects the fluoride complex here. Support comes from the large vibronic enthalpy increment $(\Delta H_5')^v$, which indicates rather soft properties of $(PF_5^{2-})_s$ due to the geometric effect—finally leading to a negative dissociation enthalpy. As expected, ΔH_5 is very small also for $(PCl_5^{2-})_s$ (Table 9), and for the bromide complex as well (0.20 eV).

We are aware that—when the complex stability toward the ablation of one ligand is discussed—the free enthalpy change should be used instead of ΔH_5. The entropy contribution is very probably negative, mainly because the number of particles increases upon dissociation. Thus, besides $(PF_5^{2-})_s$, also $(PCl_5^{2-})_s$ is expected to be unstable with regard to the respective complex with CN = 4. Nevertheless, we have included both species in the discussion.

III.2.2. $(BX_5^-)_s$ Complexes. The tendency of these complexes to distort solely by electronic forces is restricted to the fluoride and chloride complexes—similar to the situation for the bare AX_5^{2-} polyhedra (Figure 8). The iodides (not listed) have positive $\delta E_t'$ and nearly vanishing δE_t values, with obviously soft mode behavior along ϵ'-type nuclear displacements. The $\eta_{C_{4v}}$ versus N^m correlation (Figure 10b) is rather good, suggesting again decreasing lone pair instability in the sequence from the fluorides to the bromides; the cationic sequence is $S^{IV} > Se^{IV} \leq Te^{IV}$ (see section III.2.3). Table 10 reveals, similar to the situation for CN = 4 (Table 6), that N^m and $\eta_{C_{4v}}$ are—at least for the chlorides and the bromides—mostly slightly smaller for $(BX_5^-)_s$ in comparison with the $(AX_5^{2-})_s$ species. It is striking however—when $(AX_5^{2-})_s$ $[(BX_5^-)_s]$ complexes are compared with the corresponding $(AX_4^-)_s$ $[BX_4]$ species (Table 6)—that these two quantities distinctly decrease; we deduce again that an increase of the CN usually makes the polyhedra softer and the lone pair instability less pronounced. The calculated radial and angular distortions of complexes $(BX_5^-)_s$ during the $D_{3h} \rightarrow C_{4v}$ transition (Tables 7 and 8) are similar to those mentioned in section III.2.1.

Figure 11 shows as a model example the KS MO scheme of $(SeF_5^-)_s$. The $a_1'(4s^2)$ and $e'(4p_{x,y}^0)$ MOs are the HOMO and LUMO in D_{3h}—as for all considered entities with CN = 5. However, there is occasionally a complication in the C_{2v} (C_{4v}) point group; here, the highest nonbonding a_2 MO may energetically interfere with the a_1 MO resulting from the HOMO a_1' in D_{3h} such that the former becomes the HOMO—which occurs for the chlorides and bromides. Correspondingly, ionization energies refer to this MO instead of the "lone pair" MO a_1; the influence on the chemical hardness is small however, a significant reduction occurring only in the cases of $(SBr_5^-)_s$ and $(SeBr_5^-)_s$.

In agreement with the experimentally observed tendency of BX_4 molecules, in particular of $Se(Te)F_4$, to form complexes $(BX_5^-)_s$, the dissociation enthalpies according to eqs 9a and 9b adopt rather large positive values (Table 9). As in eqs 7a and 7b with the same anionic charges the solvent weakens the stability of the singly charged complex ($\delta H_5^s < 0$).

$$(BX_5^-)_s \rightarrow BX_4 + (X^-)_s \; (\Delta H_5) \qquad (9a)$$

$$BX_5^- \rightarrow BX_4 + X^- \; (\Delta H_5') \qquad (9b)$$

Though an ionic size effect is not obvious here due to DFT, the potential curves of the softer complexes are flat

Table 9. Dissociation Enthalpies (Eqs 8 and 9, eV) ΔH_5, Solvation Energies δH_5^s, and the $\Delta H_5'$ Enthalpy Increments $(\Delta H_5')^c$ and $(\Delta H_5')^v$ for Selected Complexes AX_5^{2-} (A = P, As; X = F, Cl) and BX_5^- (B = S, Se; X = F, Cl), $\Delta H_5 = \Delta H_5' + \delta H_5^s$, $\Delta H_5' = (\Delta H_5')^c + (\Delta H_5')^v$

	P, F	As, F	P, Cl	As, Cl	S, F	Se, F	S, Cl	Se, Cl
$(\Delta H_5')^c$	−1.95	−1.59	−2.13	−1.92	3.87	4.11	2.12	2.36
$(\Delta H_5')^v$	−0.94	−0.55	−0.15	−0.01	−0.85	−0.48	−0.06	0.00
δH_5^s	2.73	2.55	2.38	2.29	−1.97	−2.01	−1.19	−1.36
ΔH_5	−0.16	0.41	0.10	0.36	1.05	1.62	0.87	1.00

Table 10. Vibronic Energies (eV; See the Text for Definitions) of the PJT Interaction in Trigonal Bipyramidal $(AX_5^{2-})_s$ and $(BX_5^-)_s$ Complexes and CX_5 Molecules Possessing an s^2 Lone Pair, for the C_{2v} (C_{4v}) Ground-State Minimum[a]

complex	δE_t	$\delta E_t'$	E_{vib}^m	E_{rf}^m	E_{FC}^m	N^m	$\eta_{C_{4v}}$	$\eta_{D_{3h}}$
$(PF_5^{2-})_s$[b]	−1.14	−0.89	1.56	0.67	6.03	2.65	6.22	5.36
$(AsF_5^{2-})_s$[b]	−0.56	−0.18	0.89	0.71	5.62	2.11	5.87	5.53
$(SbF_5^{2-})_s$	−0.66	−0.18	0.91	0.73	5.47	2.03	4.74	4.74
$(BiF_5^{2-})_s$	−0.17	0.35	0.55	0.90	5.32	1.62	4.61	4.96
$(PCl_5^{2-})_s$	−0.33	−0.12	0.57	0.45	3.75	1.34	4.20	4.01
$(AsCl_5^{2-})_s$	−0.20	0.00	0.34	0.34	3.70	1.08	4.15	4.16
$(SbCl_5^{2-})_s$	−0.23	0.03	0.37	0.40	3.60	1.09	4.01	4.02
$(BiCl_5^{2-})_s$	−0.06	0.10	0.14	0.24	3.84	0.72	4.07	4.27
$(PBr_5^{2-})_s$	−0.19	−0.04	0.30	0.26	3.21	0.94	3.31	3.26
$(AsBr_5^{2-})_s$	−0.11	0.02	0.17	0.19	3.22	0.73	3.02	3.05
$(SbBr_5^{2-})_s$	−0.14	0.04	0.21	0.25	3.11	0.77	2.80	2.86
$(BiBr_5^{2-})_s$	−0.03	0.07	0.07	0.14	3.42	0.49	2.53	2.65
$(AsI_5^{2-})_s$	−0.12	0.02	0.16	0.18	2.82	0.64	2.62	2.56
$(SbI_5^{2-})_s$	−0.06	0.04	0.14	0.18	2.59	0.58	2.23	2.22
$(SF_5^-)_s$	−1.10	−1.08	1.56	0.48	5.72	2.55	6.18	5.26
$(SeF_5^-)_s$	−0.70	−0.56	1.08	0.52	5.46	2.18	5.87	5.35
$(TeF_5^-)_s$	−0.90	−0.68	1.14	0.46	5.70	2.28	5.69	5.11
$(SCl_5^-)_s$	−0.24	−0.03	0.41	0.38	3.10	1.05	3.77	3.80
$(SeCl_5^-)_s$	−0.14	−0.01	0.26	0.25	2.93	0.82	3.72	3.90
$(TeCl_5^-)_s$	−0.19	−0.05	0.34	0.29	2.94	0.94	3.75	3.79
$(SBr_5^-)_s$	−0.11	0.05	0.19	0.24	2.56	0.68	3.09	3.20
$(SeBr_5^-)_s$	−0.04	0.04	0.11	0.15	2.47	0.51	3.11	3.29
$(TeBr_5^-)_s$	−0.07	0.03	0.14	0.17	2.44	0.58	3.21	3.40
ClF_5	−0.80		1.08	0.28	3.95	1.76	5.50	4.96
BrF_5	−0.60		0.94	0.34	4.18	1.75	5.47	5.13
IF_5	−0.96		1.25	0.29	5.13	2.20	5.76	5.06

[a] The chemical hardnesses $\eta(C_{2v})$ and $\eta(D_{3h})$ are also listed. [b] Double-ζ basis.

along the $C_{4v} \rightarrow C_s$ distortion path. Interestingly enough, the geometry of one of the two $SeCl_5^-$ polyhedra in $PCl_4^+SeCl_5^-$ [35] is suspicious of such activity (Table 8). It arises, in analogy to that of $(PCl_5^{2-})_s$, from $\epsilon'(\zeta)$ displacements of mainly stretching type (Figure 2) superimposed on a C_{4v} distortion with $R_{ap} = 2.19$ Å and $R_b = 2.39$ Å ($\rightarrow C_s$, with ±0.10 Å). Shallow minima at such C_s geometry may emerge already from tiny lattice strains.

III.2.3. CF_5 Molecules. The calculated and observed geometries for the three CF_5 molecules (C^V; Cl, Br, I) are listed in Table 7. In the $\eta_{C_{4v}}$ versus N^m correlation (Figure 10b) these fluorides cover a range roughly comparable to that of the corresponding isoelectronic $(BF_5^-)_s$ and $(AX_5^{2-})_s$ complexes (Figure 10a, Table 10). Surprisingly, IF_5 exhibits the highest hardness value and largest vibronic instability of the three molecules. This can not be attributed to relativistic effects, which become more pronounced for the heavier elements on proceeding from the fifth main group to the sixth (see Te^{IV} above) and seventh main groups.

IV. Conclusions and Summary

We have investigated halides and halide complexes of the elements from the fifth, sixth, and seventh main groups with a single lone pair for CNs 4 and 5. All species possess s^2-type ground states in their parent T_d (CN = 4) and D_{3h} (CN = 5) symmetries. We have applied a vibronic coupling approach[36] to account for the lone pair influence, using DFT for the calculation of the various vibronic and restoring energies and the distortion geometries. Wherever a comparison was possible, the calculated energies and geometries are in fair agreement with available experimental data. The geometries—if a distortion occurs—are mostly near those predicted by VSEPR[4]—a butterfly-shaped C_{2v} geometry (CN = 4) close to a pseudo trigonal bipyramid, $X^{ax}{}_2Z(X_2E)^{eq}$ (E = lone pair) and a very near C_{4v} geometry (CN = 5) which approximately corresponds to a (tetragonally compressed) pseudooctahedron, X_5ZE.

A surprising structural effect is observed in the tetrahedral case for some complexes, by showing an additional deformation component superimposed on the C_{2v} geometry with two short and two long bond lengths. By shortening and lengthening either one of the two latter spacings, the geometry moves toward a 3 (short distance) + 1 (very long distance) coordination ($C_{2v} \rightarrow C_s{}^a \rightarrow i\text{-}C_{3v}$ distortion path). Though this distortion component can also be accounted for by the vibronic model, we interpret it as originating from an ionic size effect. The respective central ion is too small

(35) Neumüller, B.; Lau, C.; Dehnicke, K. *Z. Anorg. Allg. Chem.* **1996**, *622*, 1847.

(36) Reinen, D.; Atanasov, M. In *Comprehensive Coordination Chemistry II, Vol.1 Fundamentals*; Lever, A. B. P., Ed.; Elsevier: New York, 2003; Vol. 1, Chapter 1.35.

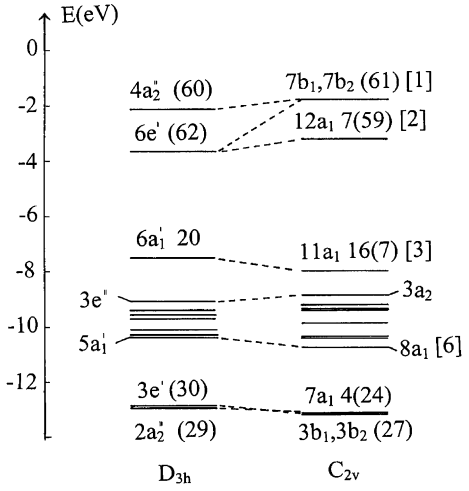

Figure 11. Kohn−Sham MO energy diagram of $(SeF_5^-)_s$ for DFT-optimized D_{3h} and C_{2v} geometries with the selenium 5s and 5p (in parentheses) and 5d (in brackets) electron density contributions. The symmetry-adapted LCAOs in D_{3h} originating from the ligand 2s and 2p AOs are $2xa_1'(\sigma)$, $e'(\sigma+\pi)$, $a_2''(\sigma+\pi)$ and $2xa_1'(\sigma)$, $e'(\sigma+\pi)$, $a_2''(\sigma+\pi)$, respectively, as well as a_2', a_2'', 2xe′, and 2xe″ (nonbonding); the Se(4s, 4p) AOs commute to $a_1'(\sigma)$, $a_{2''}(\sigma+\pi)$, and $e'(\sigma+\pi)$. The D_{3h} MOs transform in C_{2v} as follows: $a_1' \rightarrow a_1$; $a_2' \rightarrow a_2$; $a_2'' \rightarrow b_1$; $e' \rightarrow a_1 + b_2$; $e'' \rightarrow a_2 + b_1$. The only weakly bonding $a_1'(\sigma)$, $e'(\sigma+\pi)$, and $a_2''(\sigma+\pi)$ MOs from 2s (F) at ∼−28.4 eV and the bonding $4a_1'$ MO with 66% 4s Se character at −19.7 eV are not shown; the C_{2v} split components of the nonbonding MOs are partly depicted.

for CN = 4, thus driving the geometry toward a reduced CN (Table 4). Similarly, the compressed tetragonal pyramid of a CN = 5 complex may analogously display a superimposed instability—yielding a polyhedron with one very long spacing and otherwise an (approximately) butterfly-shaped complex of CN = 4. In particular $(PX_4^-)_s$ and $(PX_5^{2-})_s$ complexes behave in such a way (Tables 4 and 8, Figure 9). We have further studied the dynamic interrelation between the various possible geometries in the vibronic landscape for a selected number of molecules and complexes with CN = 4 (Table 3, Figure 6). For example, it is shown that the fluxionality ("ligand interchange") of some species occurs via a C_{4v} transition state (Berry mechanism, SF_4, $(PF_4^-)_s$), while for others a C_s transition state is energetically more favorable (lever mechanism, SCl_4, $(PCl_4^-)_s$). Low-lying relative energy minima may also gain influence on the reactivity; thus, the vibronically stabilized *i*-C_{3v} geometry makes BX_4 molecules sensitive toward the formation of BX_3^+ cations, when supported by the presence of Lewis acids.

To simulate the real situation as close as possible, we have included a polarizable solvent continuum in the DFT calculations on the charged complexes (and frequently also in the case of neutral molecules) to approximately account for the presence of counterions in a crystal lattice or of solvent molecules. The general effect is a stabilization of the distorted structure, because—due to the generally larger dipole moment—the solvent−complex interaction is more pronounced with the distorted entity. By the solvent energy many complexes, which would be stable versus lone pair deformations otherwise, undergo distortions with flat potential energy minima—exhibiting soft mode properties along the vibronically active displacement coordinates and hence

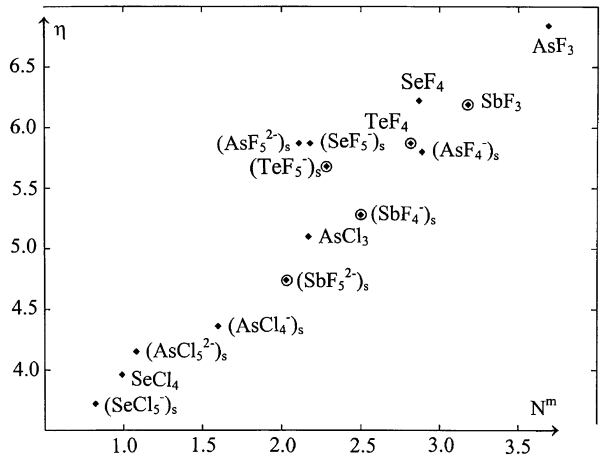

Figure 12. Correlation of the chemical hardness η ($\eta_{C_{3v}}$, $\eta_{C_{2v}}$, $\eta_{C_{4v}}$ for CN = 3−5, respectively) and the vibronic coupling energy (N^m) for selected molecules and complexes, illustrating the hardness rule (species with isoelectronic cations from different main groups—As^{3+}, Se^{4+} and Sb^{3+}, Te^{4+}—are marked by the same symbol).

sensitivity toward lower-symmetry strains from the second-sphere environment[15] in a crystal lattice, for example.

The chemical hardness η, as an observable quantity, has been found to directly mirror the tendency of a lone pair complex to distort. This is so because the strength of the vibronic coupling, represented by N^m, is closely correlated with η.[5,6] If one proceeds from the harder to the softer ligands $F^- \rightarrow I^-$, the resistance toward lone pair distortions increases distinctly. A significant result of the present study is that *the vibronic coupling energy and the chemical hardness decrease, if the CN becomes larger* (Figures 4 and 10). Specifically, while all AX_3 molecules distort ($D_{3h} \rightarrow C_{3v}$), only the larger part of the $(AX_4^-)_s$ complexes and BX_4 molecules does so ($T_d \rightarrow C_{2v}$) (Figure 3); the species with CN = 5, $(AX_5^{2-})_s$, $(BX_5^-)_s$, and CX_5 ($D_{3h} \rightarrow C_{4v}$), resist lone pair distortions to an even larger extent (Figure 8). The large group of complexes with CN = 6 finally retains mostly the O_h parent geometry.[6] Accordingly, we deduce from Figure 12 sequences from hard to soft, such as $SbF_3 \rightarrow (SbF_4^-)_s \rightarrow (SbF_5^{2-})_s$, $AsCl_3 \rightarrow (AsCl_4^-)_s \rightarrow (AsCl_5^{2-})_s$, or $SeF(Cl)_4 \rightarrow (SeF(Cl)_5^-)_s$—with a small inconsistency in the series from AsF_3 via $(AsF_4^-)_s$ to $(AsF_5^{2-})_s$. The comparison of isoelectronic species with central ions from different main groups (A^{III}, B^{IV}, C^V) lacks definiteness. Refraining from such an attempt, we are nevertheless left with a clean correlation of the chemical hardness with the susceptibility to distort by lone pair influence, which we refer to as the hardness rule. The latter is well in accord with the experimental evidence.[1,2]

The vibronic coupling model—using simple group-theoretical arguments—yields precise knowledge about all vibronically active vibrational modes (Figures 1 and 2). Together with DFT it provides information about the involved energetics and dynamics—for the ground state, but for near-lying excited states as well (Figures 5 and 11, Tables 6 and 10). Furthermore, predictions of whether a species will distort or not are possible. The exact knowledge of the distortion pathways and their energetics is a great advantage as compared to the simple VSEPR concept. In all cases,

which are not touched by the ionic size effect, the lone pair deformation either occurs along the axis of highest symmetry (CN = 4, S_4) or aims at the highest possible distortion geometry (CN = 5, C_{4v}). *The driving force for the lone pair effect is the gain in the covalent binding energy upon distortion*[17,6] and not—in some contrast to the VSEPR[4] and ligand close packing (LCP)[37] model—the interpair and/or Pauli closed shell repulsion.

Acknowledgment. We owe thanks to the Deutsche Forschungsgemeinschaft (DFG) for financial support.

Appendix: Remarks on the Origin of the Hardness Rule

The chemical hardness η[9] is directly accessible from the first ionization potential (I) and the electronic affinity (A) of the considered molecular or complex species in the distorted geometry (eq A1). I, A, and η are correlated with the HOMO and LUMO Kohn–Sham energies ϵ_{HOMO} and ϵ_{LUMO} and the respective Coulomb repulsion energies C_{HOMO} and C_{LUMO} via eqs A2 and A3.

$$\eta \approx (I - A)/2 \tag{A1}$$

$$I = -\epsilon_{HOMO} + C_{HOMO}, \quad A = -\epsilon_{LUMO} - C_{LUMO} \tag{A2}$$

$$\eta = (1/2)[(\epsilon_{LUMO} - \epsilon_{HOMO}) + (C_{HOMO} + C_{LUMO})] \tag{A3}$$

The MO energy difference $\epsilon_{LUMO} - \epsilon_{HOMO}$ is very close to the many-electron Franck–Condon energy (E_{FC}^m), which, in the strong vibronic coupling limit, equals $2N^m$ (eqs 5a and 5b). η is thus made up of N^m and a Coulomb contribution, $(1/2)(C_{HOMO} + C_{LUMO}) \equiv C$. The latter increases in the series from iodide to fluoride; i.e., it follows the same trend as the chemical hardness does. This is shown by the (nonlinear) C/N^m correlation for AX_3 molecules as model examples in Figure 13. Obviously the C term enlarges the increase of η with respect to N^m considerably. The interesting result is that the interelectronic repulsion—which gets smaller with increasing electron delocalization and hence covalency (nephelauxetic effect)—is also indicative for the vibronic coupling energy. The singular exception from the correlation in Figure 13 is PF_3, as are (less pronounced) the complexes $(PF_4^-)_s$ and $(PF_5^{2-})_s$. The origin is perhaps an anomalously large change in overlap upon distortion in these cases.

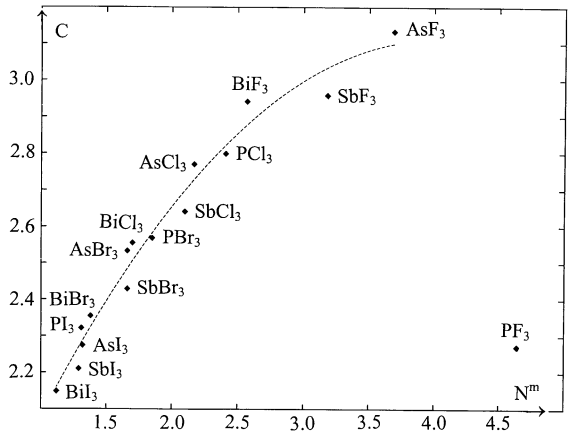

Figure 13. Correlation between the interelectronic repulsion increment C and the vibronic coupling energy N^m (eV) for C_{3v}-distorted AX_3 molecules: DFT data, squares; fit (without PF_3) to a quadratic polynomial $C = 1.274 + 0.921(N^m) - 0.116(N^m)^2$ (standard deviation 0.047 eV), hatched curve.

Note Added after ASAP: The version of this paper posted ASAP on February 5, 2004, contained errors in Table 8 and subsection III.2.3. These errors were corrected in the version posted ASAP on February 16, 2004.

IC030214S

(37) Robinson, E. A.; Gillespie, R. J. *Inorg. Chem.* **2003**, *42*, 3865.